

Impact of rotation on synthetic mass-radius relationships of two-layer rocky planets and water worlds

J.-M. Hure¹, P. Noé^{1,2}, C. Staelen¹, and E. Di Folco¹

¹ University of Bordeaux, CNRS, LAB, UMR 5804, F-33600 Pessac, France
e-mail: jean-marc.hure@u-bordeaux.fr

² LPC2E, OSUC, Univ Orleans, CNRS, CNES, Observatoire de Paris, F-45071 Orleans, France

Received ??? / Accepted ???

ABSTRACT

We have analyzed the effects of rotation on mass-radius relationships for single-layer and two-layer planets having a core and an envelope made of pure materials among iron, perovskite and water in solid phase. The numerical surveys use the DROP code updated with a modified polytropic equation-of-state (EOS) and investigate flattening parameters f up to 0.2. In the mass range $0.1 M_{\oplus} \lesssim M \lesssim 10 M_{\oplus}$, we find that rotation systematically shifts the curves of composition towards larger radii and/or smaller masses. Relative to the spherical case, the equatorial radius R_{eq} is increased by about $0.36f$ for single-layer planets, and by $0.30f$ to $0.55f$ for two-layer planets (depending on the core size fraction q and planet mass M). Rotation is an additional source of confusion in deriving planetary structures, as the radius alterations are of the same order as i) current observational uncertainties for super-Earths, and ii) EOS variations. We have established a multivariate fit of the form $R_{\text{eq}}(M, f, q)$, which enables a fast characterisation of the core size and rotational state of rocky planets and ocean worlds. We discuss how the observational data must be shifted in the diagrams to self-consistently account for an eventual planet spin, depending on the geometry of the transit (circular/oblate). A simple application to the recently characterized super-Earth candidate LHS 1140 b is discussed.

Key words. Equation of state - Methods: analytical - Methods: numerical - Planets and satellites: composition - Planets and satellites: interiors - Planets and satellites: terrestrial planets - Planets and satellites: oceans - Stars: individual: 2MASS J00445930-1516166 - Techniques: photometric - Techniques: radial velocities

1. Introduction

The great diversity of exoplanets — more than 5700 objects detected over the last three decades — represents a remarkable challenge for models of internal structure, scenarios of planetary formation and mechanisms at work, and detection methods (Haswell 2010; Nielsen 2022). The opportunity to find planets resembling Earth, and possibly hosting forms of life, has become an attractive reality (Léger et al. 2004; Schwietzman et al. 2018; Wandel 2018; Rigby & Madhusudhan 2024; Lichtenberg & Miguel 2025). When transit and Doppler spectroscopy can be combined together, the radius R and mass M of the planet are measured with relatively good precision (e.g. Spiegel et al. 2014; Agol et al. 2021). The resulting mean mass-density $3M/4\pi R^3$ and the inspection of the planet position in pre-computed mass-radius diagrams bring informations in terms of chemical/mineralogical composition. Unfortunately, the knowledge of these data is far from sufficient to infer a unique internal structure, because the inverse problem is highly degenerate. There is a certain diversity of equation-of-states due to the variety of materials present at the period of formation, and the thermodynamical conditions are complex. The number of internal layers is another important unknown. Key informations linked to the planet environment and age of the system can also be considered to discriminate between plausible configurations and unlikely ones. In particular, the proximity of the parent star sets severe constraints in terms of chemical composition (Dorn et al. 2017; Brugger et al. 2017), stellar wind, instellation and heat transport (Valencia et al. 2006; Wagner et al. 2012; Yunsheng

Tian & Stanley 2013; Mousis et al. 2020; Aguichine et al. 2021; Haldemann et al. 2024), tides towards synchronization (Valencia et al. 2007b; Nettelmann et al. 2011; Kellermann et al. 2018). Realistic models including all these ingredients together are a formidable technical challenge.

To our knowledge, mass-radius relationships for planets (solid or even gaseous) are in general computed in the spherical/static limit. But planets rotate, more or less. It is hard to conceive that all exoplanets are either perfect spheres with no proper spin, or completely tidally locked with their parent star. Planets in our Solar System are good examples of objects exhibiting slow to moderate rotations. When the orbital separation is short, substantial three-dimensional deformations are expected (e.g. Chandrasekhar 1933b). For planets moving on large orbits, the spin-orbit resonance may not be reached, depending on the age of the system. The time scale actually varies with the separation a and stellar mass M_{\star} as a^6/M_{\star}^2 (e.g. Goldreich & Peale 1968; Zahn 1989; Leconte et al. 2015; Barnes 2017). Accretion of gas and dust in a circumstellar disc is efficient in spinning up planetary embryos (e.g. Mitra 1977). Young planets are expected to rotate very fast, in particular due to accumulation of angular momentum from pebble accretion and collisions. Small size bodies like asteroids are highly affected by stochastic collisions and may end up with small rotation periods, of the order of a few hours (Farinella et al. 1992). In the giant impact theory, the rotation period of the proto-Earth is estimated to 2.7–5.8 h (pre- and post-impacts), and the polar-to-equatorial axis ratio $R_{\text{pol}}/R_{\text{eq}}$ of the spheroidal Earth should have been well below unity, close

to the mass-shedding limit/break-up velocity (de Meijer et al. 2013; Canup 2012).

Another motivation for considering rotation comes from the increasing interest for the detection of oblateness in transit light-curves (Akinsanmi et al. 2020; Carado & Knuth 2020; Liu et al. 2025). The photometric signal from a transiting planet depends on the planet size relative to the star size, and to the orbital separation (Haswell 2010). Again, the planet is generally assumed spherical, which means that area blocking the stellar flux towards the observer is a circular disc. The existence of oblateness introduces a bias when retrieving the planets parameters, in particular the radius (Berardo & de Wit 2022). With present-day photometric sensitivity and time-sampling, the systematic detection of oblateness during the ingress/egress phases of transits is marginally accessible for gaseous planets, which represent the best targets (Zhu et al. 2014; Liu et al. 2024). In contrast, rocky planets and water worlds that have not reached synchronisation yet orbit at large separation are out of the range of detection for the transit method. In the perspective of finer measurements (in terms of timing and relative flux) and future instruments like the Plato mission, there is a great interest in anticipating and understanding the role of rotation in mass-radius relationships, and in quantifying the additional level of confusion it brings in interpreting data.

Estimating the change in the radius and/or mass of a self-gravitating fluid due to rotation is an old problem. For a homogeneous spheroid with flattening $f \equiv 1 - R_{\text{pol}}/R_{\text{eq}} \ll 1$, the equatorial radius is larger than for a sphere having the same mass by the quantity $\Delta R_{\text{eq}} \approx +\frac{1}{3}R_{\text{eq}}f$. In similar conditions, for a given equatorial radius, the mass of the rotating spheroid is smaller than for the sphere by $\Delta M \approx -Mf$. It means that for an incompressible body with flattening $f = 3\%$ (a little bit higher than for Neptune and Uranus), the relative deviation in the radius reaches $\Delta R_{\text{eq}}/R_{\text{eq}} \approx 1\%$, which value is comparable to the precision obtained by the transit method. Solid planets are not homogeneous spheroids. The modification in the structure due to rotation has been treated in the limit of weak distortion by Chandrasekhar (1933a) for a polytropic EOS where the pressure P and the mass-density ρ scale as $P \propto \rho^\gamma$. The result depends on the properties on Emden's function at the equator (in particular, the non-analytical derivative), and especially on the polytropic exponent γ of the gas. As rotation increases, the equatorial elongation changes faster than the pole contracts. For a given mass, the central density is slightly reduced; see also Williams (1988), Vavrukh & Dzikovskiy (2020) and Ricard & Chambat (2024) for $\gamma = 2$. How ΔR_{eq} and ΔM are modified for rocky planets and water worlds? And how these changes caused by rotation compare with observational error bars δR and δM ? In this article, we investigate the impact of rotation on synthetic, single-layer and two-layer planets with internal composition typical of the Earth (iron/silicate) and water-rich planets. The case of planets supporting an atmosphere is planned for another paper.

Authorizing rotation renders the problem technically much more complex than in the static/spherical case, as there are two spatial coordinates to manage simultaneously, instead of a unique, radial variable. For this reason mainly, we deliberately abandon some "ingredients" that are undoubtedly decisive in any realistic approach. We assume single-layer and two-layer solid planets in rigid rotation, without any atmosphere. The radius is greatly changed in the presence of a relatively massive atmosphere (Adams et al. 2008; Howe et al. 2014). Regarding the EOS, there are several degrees of sophistication and realism, especially when the temperature is an explicit parameter (Swift et al. 2012; Hakim et al. 2018; Boujibar et al. 2020). For sim-

plicity, we use a barotropic EOS appropriate to rocky/icy planets, in the form of the modified polytrope, according to Seager et al. (2007). This is a reliable approximation to more complex ansatz. In this context, different mineralogical compositions can be considered, from pure to impure materials. We have selected only three kinds of materials, namely iron, silicate and water (all in solid phase). We also assume that the parent star is far enough, and therefore neglect the effects of tides (gravitational attraction and internal energy release) and irradiation that produce surface heating and trigger circulation caused by temperature imbalance at the surface (e.g. Auclair-Desrotour et al. 2024). We assume rigid body rotation, which is a common hypothesis.

In Sect. 2, we briefly summarize the assumptions and equation set relevant to model a multi-layer planet in rotation, which are mostly described in Basillais & Huré (2021), and the main properties of the DROP code used to numerically solve the equilibrium on a cylindrical (R, Z) -grid (see also Huré & Hersant 2017; Huré et al. 2018). Attention is paid to the specific link between the enthalpy H and the mass-density ρ associated to the EOS. Sections 3 and 4 are devoted to an exploration of the parameter space in the single-layer case and two-layer case, respectively. Note that there are two key parameters, namely the core fractional size $q \in [0, 1]$ and the flattening $f = 1 - R_{\text{pol}}/R_{\text{eq}}$. In particular (see Sect. 1.1), we take the liberty to investigate the influence of rotation on mass-radius relationships well beyond the standard limit of slow rotations, by considering flattening parameters f up to 0.2 (simulations can go much above). A global fitting procedure is performed, leading to a general, fully reversible formula of the form $R_{\text{eq}} = R_{\text{eq}}(M, q, f)$, mixing quadratic laws and a sigmoid. In Sect. 5, we discuss the diversity of structures in terms of δq and δf compatible with observational error bars δM in the mass and δR_{eq} in the radius. Although this is not the nominal target regarding our purpose, we consider LHS 1140 b (Dittmann et al. 2017; Ment et al. 2019; Lillo-Box et al. 2020; Cadieux et al. 2024a), a potential ocean world that has been recently modelled by Rigby & Madhusudhan (2024) and Daspute et al. (2024). The main results are summarized in the conclusion, including an example of bias correction appropriate for both circular and oblate transits. A few perspectives and possible improvements of the present work are listed.

2. Single-layer and two-layer equilibrium configurations from the Self-Consistent-Field method and the DROP code

2.1. Equation set

The structure of an isolated, spherical planet in steady state is obtained, like for stars, by integrating the one-dimensional equation for hydrostatic equilibrium, in which local gravity force balancing the pressure gradient is directly available from Gauss's theorem. The integration proceeds from the center/surface towards the opposite boundary, and shots are repeated until the boundary conditions are fulfilled, optionally with interior matching points (Cox & Giuli 1968; Haldemann et al. 2024). With this technique, it is relatively easy to incorporate various details in the physical and chemical processes, depending on the local conditions (Slattery 1977; Guillot 1999; Verhoeven et al. 2005; Seager et al. 2007; Rigby & Madhusudhan 2024). In the presence of rotation, the equation of hydrostatic equilibrium and the Poisson equation involve two spatial coordinates, and the shooting methods are less direct. If the rotation rate Ω inside the planet depends only on the cylindrical distance R from the axis of rotation and the fluid is a barotrope (e.g. Amendt et al. 1989), then the two com-

ponents of the Euler equation are the gradient of the following scalar field

$$H + \Psi + \Phi = \text{const.}, \quad (1)$$

where $\Phi = -\int \Omega^2 R dR$ is the centrifugal potential, $H = \int dP/\rho$ is the enthalpy, ρ is the mass density, P is the pressure, and Ψ is the gravitational potential, which obeys the Poisson equation

$$\Delta\Psi = 4\pi G\rho. \quad (2)$$

The problem then consists in finding H satisfying these two equations at each point in the fluid, and this is usually performed via an iterative procedure, known as the Self-Consistent-Field (SCF) method. The enthalpy H is guessed, then Ψ is computed from Eq.(2) by using $\rho(H)$, and it is injected in Eq.(1) to get the enthalpy H . This new field is compared to the previous one, and the cycle is repeated until convergence. A wide literature has been devoted to the determination of the solutions for Eq.(1), in various contexts, in particular assuming a polytropic EOS for the material where $P \propto \rho^\gamma$ (e.g. Hachisu 1986; Horedt 2004). A new difficulty arises when combining rotation and layering, due to the presence of mass-density jumps (e.g. Kiuchi et al. 2010; Schubert et al. 2011; Kadam et al. 2016; Basillais & Huré 2021; Houdayer & Reese 2023). Actually, when the body is made of \mathcal{L} well-differentiated layers in total, and provided the two conditions above are still satisfied, then there is one Bernoulli equation per layer to consider, because each layer has its own EOS. The gravitational potential is still defined by Eq.(2), but the second member becomes a piece-wise function. Pressure balance at each interface S_l bounding layers $l \in [1, \mathcal{L}]$ and $l + 1$ writes

$$P_l|_{S_l} = P_{l+1}|_{S_l}, \quad (3)$$

means that the knowledge of all interfaces is mandatory (layer $\mathcal{L} + 1$ denotes the free space). In total, there are $2\mathcal{L} + 1$ equations to solve simultaneously. We proceed according to Basillais & Huré (2021), by solving one Poisson equation per layer on a dedicated computational grid with appropriate boundary conditions, namely $\Delta\Psi_l = 4\pi G\rho_l$, and the total potential Ψ is obtained by superposition. This is well adapted to treat correctly mass-density jumps at the interface between layers.

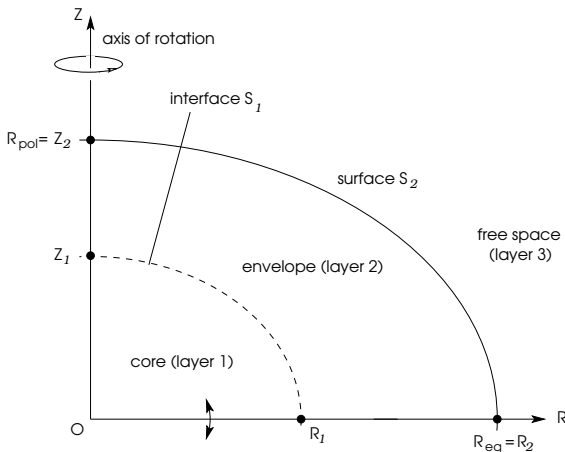


Fig. 1. Typical configuration and notations for a rotating system made of $\mathcal{L} = 2$ differentiated layers: the core (C) as layer 1, and the envelope (E) as layer 2. The polar radius is $R_{\text{pol}} \equiv Z_2$ and the equatorial radius is $R_{\text{eq}} \equiv R_2$. All layers rotate at the same rate Ω around the Z -axis.

As mentioned in the introduction, we consider single-layer and two-layer planets. For $\mathcal{L} = 2$, the core (C) is layer 1, and the

envelope (E) is layer 2 as depicted in Fig. 1. The equatorial and polar radius of the core are R_1 and Z_1 respectively, and we have $R_2 \equiv R_{\text{eq}} \geq R_1$ and $Z_2 \equiv R_{\text{pol}} \geq Z_1$ for the envelope. Usually, rotation flattens the structure so that we expect $Z_l \leq R_l$. The two layers are in rigid rotation at the same rate Ω .

2.2. The modified polytropic EOS and the selection of mineralogical compositions for solid planets

As the diversity of planetary interiors is wide, the coverage in mass-density, pressure and temperature must be sufficient (e.g. Yunsheng Tian & Stanley 2013; Hakim et al. 2018; Boujibar et al. 2020; Haldemann et al. 2020). For telluric and ocean planets with masses in the range $0.1M_{\oplus}$ to $10M_{\oplus}$, different EOS can be selected (e.g. Grasset et al. 2009; Spiegel et al. 2014; Ricard & Chabmat 2024); see Sect. I.1. These are generally combinations of experimental data and theoretical calculations, and consist of piece-wise functions and tables of data specific for various phases. Our primary objective is to test the role of rotation and to simplify the problem as much as possible. In this context, we work with the barotropic EOS given by Seager et al. (2007), namely

$$P = K(\rho - \rho_s)^{1/m} \quad (4)$$

where ρ_s is the mass-density at null pressure, K and m are constants¹. This analytical model works for several types of solid materials, in particular for water, silicates and iron, and it includes quantum effects important at very high pressures (Zapolsky & Salpeter 1969). It is well suited to bodies with central pressures from 10^{11} to $10^{13.5}$ dyn/cm², expected for the mass range of interest here (Cox & Giuli 1968); see also Sect. 3.4.

The parameters m , ρ_s and K needed in Eq.(4) are listed in Tab. 1 for solid iron (I), perovskite (P) and water (W), following Seager et al. (2007). The table also contains the index n and the exponent $\gamma = 1 + \frac{1}{n} = \frac{1}{m}$ corresponding to the high-pressure limit. Regarding water, we are aware that $\rho_s = 1.46$ g/cm³ is larger than the standard values for ice and liquid phase in standard conditions, but we follow the authors' prescription for the sake of consistency.

If we consider only configurations where $\rho_s(E) < \rho_s(C)$, including the unrealistic case of an iron core and a water envelope, there are six different possibilities:

- $C \in \{I, P, W\}$ for single-layer planets,
- $CE \in \{IP, IW, PW\}$ for two-layer planets.

2.3. The associated enthalpy

With respect to a polytropic EOS where $P \propto \rho^\gamma$ and $\gamma = 1 + \frac{1}{n}$, the bimodal prescription advantageously incorporates the incompressible case $n = 0$ (i.e. $\gamma \rightarrow \infty$) at vanishing/low pressure and a compressible case at high pressure, with $\gamma \rightarrow \frac{1}{m}$. With Eq.(4), this change is especially significant in terms of the associated enthalpy H required in Eq.(1), as we have

$$H(\rho) = \gamma K \int (\rho - \rho_s)^{\gamma-1} \frac{d\rho}{\rho}. \quad (5)$$

¹ The notation differs slightly from Seager et al. (2007) where Eq. (4) is written as $\rho = \rho_0 + cP^m$. The connection between the two formula requires $\rho_0 \rightarrow \rho_s$, $n \rightarrow m$ and $c \rightarrow K^{-m}$. As a consequence, if the pressure P is measured in dyn/cm², then the values of K^{-m} reported in Tab. 1 are in g/cm³ × (dyn/cm²)^{-m}.

Table 1. Data* for the modified EOS from Seager et al. (2007), according to Eq.(4).

| | ρ_s (g/cm ³) | K^{-m} | m | index n | exponent γ | $\frac{1-n}{3-n} \equiv \beta$ |
|------------|-------------------------------|---------------------------|-------|-----------|-------------------|--------------------------------|
| iron | 8.30 | 1.034726×10^{-6} | 0.528 | 1.11864 | 1.89393 | -0.06306 |
| perovskite | 4.10 | 0.463261×10^{-6} | 0.541 | 1.17864 | 1.84842 | -0.09809 |
| water | 1.46 | 0.954465×10^{-6} | 0.513 | 1.05338 | 1.94931 | -0.02743 |

*The coefficient K is given in g/cm³ × (dyn/cm²)^{-m}, and assumes that P is in dyn/cm² (see note 1). Coefficients n and $\gamma = 1 + \frac{1}{n}$ are computed in the limit of high pressures, i.e. $\gamma = \frac{1}{m}$.

Unfortunately, a close form for H exists only for certain values of m . For instance, for $m = \frac{1}{2}$, the enthalpy is of the form $H \sim \rho - \text{const.} \times \ln \rho$. In the general case, H is given by

$$H = K\rho_s^{\gamma-1}u^\gamma {}_2F_1(\gamma, \gamma; \gamma + 1; u) + \text{const.}, \quad (6)$$

where ${}_2F_1$ denotes the Gauss hypergeometric function, and

$$u = 1 - \frac{\rho_s}{\rho} \leq 1. \quad (7)$$

The non-linear change of variable (a Pfaff transformation) ensures that the hypergeometric series unconditionally converges since $\rho \geq \rho_s$ in the structure. It can be verified that, in these conditions, $H(\rho)$ remains bijective, and it can therefore be inverted to get $\rho(H)$. This inversion, which is accomplished by numerical means, is unavoidable since ρ is directly required to get the potential Ψ from the Poisson equation. The integration constant in Eq.(6) is of fundamental importance (there is one such constant per layer). It represents the enthalpy of the material at zero pressure, i.e. for $u = 0$. If we define

$$A = \frac{\rho_s}{\rho_0} \leq 1, \quad (8)$$

where ρ_0 is, for instance, the largest value in the actual layer, then $u_0 = 1 - A$ and so the integration constant in Eq.(6) is

$$\text{const.} = H_0 - K\rho_0^{\gamma-1}A^{\gamma-1}u_0^\gamma {}_2F_1(\gamma, \gamma; \gamma + 1; u_0). \quad (9)$$

2.4. Simulations of rotating two-layer planets at equilibrium with the updated DROP code

We use the DROP-code to determine numerically the equilibrium state of a rotating body made of \mathcal{L} layers (Basillais & Huré 2021) from the Self-Consistent-Field (SCF) method. The code is scale-free. In particular, we set $\tilde{\rho} = \rho/\rho_0$ for the mass density, and $\tilde{H} = H/H_0$ for the enthalpy, where ρ_0 and H_0 is specific to each layer. In the new version of the code, the modified polytropic EOS defined by Eq.(4) is implemented. The critical point is the automatic detection, at each step of the SCF-cycle, of the core-envelope interface S_1 where Eq.(3) has to be fulfilled; see Fig. 1. Running a simulation with the DROP code requires 3 input parameters for $\mathcal{L} = 2$:

- the flattening parameter $f = 1 - R_{\text{pol}}/R_{\text{eq}} \geq 0$,
- the parameter $A = \rho_{s,\mathcal{L}}/\rho_{\mathcal{L}}^{\text{bottom}} \leq 1$ which sets the top-to-bottom mass-density ratio in the surface layer,
- the relative size of the core $q = Z_1/R_{\text{pol}}$ along the Z -axis.

For a single-layer planet, A is basically the surface-to-center mass density ratio and the last parameter is useless. The value of this parameter mostly determines the mass of the planet. For $A \approx 0.3 - 0.85$, we typically scan two decades in mass around one Earth mass, depending on the composition.

Table 2. Results for the two-layer, IP planet displayed in Fig. 2.

| ▼ input | |
|--|---------|
| flattening parameter f | 0.05 |
| $A = \rho_{s,2}/\rho_2^{\text{bottom}}$ | 0.69689 |
| relative core size (pole) q | 0.5 |
| ▼ output | |
| equatorial radius R_{eq} in R_{\oplus} | 0.99621 |
| total mass M in M_{\oplus} | 1.00000 |
| relative mass of the core M_1/M | 0.24305 |
| central-to-mean mass-density ratio $\rho_c/\langle\rho\rangle$ | 2.14162 |
| top-to-central mass density ratio (core) $\rho_1^{\text{top}}/\rho_c$ | 0.88047 |
| rotation period T (h) | 6.36260 |
| relative size of the core (equator) Q | 0.49404 |
| interface mass-density jump $\rho_1^{\text{top}}/\rho_2^{\text{bottom}} \equiv \alpha$ | 1.88106 |
| central-to-surface mass density ratio $\rho_c/\rho_{s,2}$ | 3.06567 |
| central pressure P_c (10^9 dyn/cm ²) | 2696.31 |
| interface pressure $P_i \equiv P(Z_1)$ (10^9 dyn/cm ²) | 1488.09 |

At convergence, the code delivers the enthalpy at equilibrium $H_l(R, Z)$ for each layer $l = \{1, 2\}$, the interface S_1 and S_2 , in the form of discrete values $\{R_i, Z_i\}$, the rotation rate Ω , and the equatorial radius R_{eq} . From these data, we can compute the mass M_l of each layer, the total mass M , the core mass-fraction M_1/M , the central pressure P_c , the rotation period T , etc. (see below). The accuracy of simulations is mainly controlled by the numerical resolution. We work with $N + 1 = 129$ grid nodes per direction, with uniform spacing. This is a moderate resolution. As the quadrature and finite difference schemes are second-order accurate in the unit-square grid, the relative precision in output quantities (mass, volume, Virial parameter, etc.) is $1/N^2 \approx 10^{-4}$, typically. Most outputs are given with 5 digits.

2.5. An example of simulation

We show in Fig. 2 the pressure and mass-density profiles obtained for a two-layer planet made of an iron core and a perovskite envelope, i.e. CE=IP. For this run, we take $q = 0.5$ and $f = 0.05$. The last parameter $A \approx 0.697$ has been selected such that we get a planet with $M \approx 1M_{\oplus}$. This example therefore represents a very simplified Earth, but with flattening parameter f comparable to Jupiter's value (instead of ≈ 0.003). We see the smooth connection of the pressure at the interface, while the mass-density undergoes a jump, as expected. The output data are gathered in Tab. 2. The resulting equatorial radius is about 6346 km, and this is 6029 km at the pole. The rotation period is about 6 h 22 min.

2.6. Sampling for the numerical surveys. Tables

We have run the DROP code in the same conditions as in the previous example, by varying f , A , and q independently to each

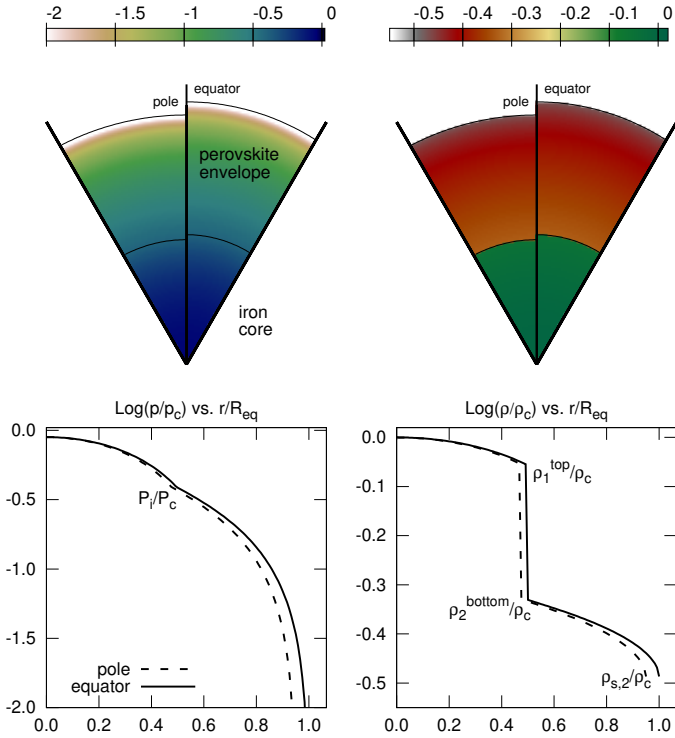


Fig. 2. Normalized pressure (*left*) and mass-density (*right*) in color code (*top panels*) close to the pole and to the equator for a two-layer, IP planet computed with the DROP code. The input/output parameters are in Tab. 2. Profiles along the rotation axis (spherical radius $r \equiv Z$) and along the equator ($r \equiv R$) are also shown (*bottom panels*).

other. Given the moderate resolution (see above), a good compromise between the computing time and the quality of the data on output is obtained with the following samplings:

- $f \in [0, 0.2]$, with $\Delta f = 0.025$ ($f = 0$ is for the static case),
- $A \in [0.05, 0.95]$ with $\Delta A = 0.025$,
- $q \in]0, 1[$ for two-layer planets, with $\Delta q = 0.1$.

This represents 171 runs for a single-layer planet, and 1536 runs in a two-layer case. As we have five different configurations (see Sect. 2.4), the number of runs amounts to 5130 in total. The list of input/output is given in the Appendix A together with a sample of data obtained for a water planet and for a IW-planet and $q = 0.5$, with $f = 0.1$ in both cases. The full tables obtained for the six types of planets are available in electronic form on Zenodo²

3. Results in the single-layer case

Before considering configurations with $\mathcal{L} = 2$, it is instructive to examine first the case where the planet is a single-layer body made of pure material, i.e. $C \in \{I, P, W\}$. The mass-radius relationships obtained for $f \in \{0, 0.1, 0.2\}$ are displayed in Fig. 3. In the static case, we have $R_{\text{eq}}(W) > R_{\text{eq}}(P) > R_{\text{eq}}(I)$ for a given mass, which is expected from the mass density of the species. We find that:

² DOI:10.5281/zenodo.15397897. Specific runs can be provided upon request. The presence of ${}_2F_1(u)$ in Eq.(6) largely increases the computing time with respect to a standard polytropic EOS (see Sec. B for a discussion about convergence acceleration and the computing time). The production of each cube of data requires about 6 h of computation on a standard computer for a two-layer configuration.

- decreasing ρ_s shifts the pure-composition lines quasi-horizontally, towards low masses (i.e. a left shift in the plane),
- decreasing the constant K^{-m} shifts the pure composition lines towards large radii and high masses (a rightward and upward shift)
- decreasing the power-law index m has a similar effect as decreasing the gaz constant.

In the graph, we have also reported the semi-empirical mass-radius relationship computed in Zeng et al. (2016) based on the Preliminary reference Earth model (Dziewonski & Anderson 1981), the data computed by Haldemann et al. (2020) from the AQUA-EOS for water (assuming a 300 K surface temperature), and the results by Fortney et al. (2007) for pure water and pure silicate planets. Given the differences in the EOS and models of internal structure with these authors (explicit treatment of temperature and heat transport mainly), the comparisons with these authors are indeed satisfactory in the spherical case. Besides, we have checked that the agreement with Fortney et al. (2007) is much better for the water line by setting $\rho_s \approx 1 \text{ g/cm}^3$ in the code.

3.1. Trends and fits

We observe that changing f at constant mass (radius) shifts the equatorial radius (mass, respectively) towards larger (lower, respectively) values, which is the consequence of the deficiency of matter along the rotation axis, i.e. $R_{\text{pol}} < R_{\text{eq}}$. The mass-radius relationships obtained for different values of f are parallel to each other, with a relatively linear/regular spacing (in log. scale). The slopes are clearly not very sensitive to rotation. However, the immediate consequence is that rotation introduces a confusion for interpreting observations, in the sense that a “high” position in the plane can correspond to a static planet with light elements, or to a rotating planet with heavy compounds. The curves are monotonic and smooth, and can clearly be fitted by simple functions. A significant curvature in the mass-radius relationship appears beyond about 10 Earth masses (see below). This is the reason why, in the following, fits are constructed by using only data falling in the reference mass-range $0.1 M_{\oplus} \lesssim M \lesssim 10 M_{\oplus}$. In terms of radius, this roughly corresponds to $0.4 R_{\oplus} \lesssim R_{\text{eq}} \lesssim 3. M_{\oplus}$. This domain is much smaller than in Seager et al. (2007), and slightly extends into the domain of gaseous planets (Edmondson et al. 2023). In these conditions, the mass-radius relationship can be well fitted by a quadratic law

$$y(x) = c_0 + c_1 x + c_2 x^2, \quad (10)$$

where $x \equiv \log M/M_{\oplus}$ and $y \equiv \log R_{\text{eq}}/R_{\oplus}$. Much better functions can indeed be found, in particular a sum of power laws in y , but a second-order polynomial is easily reversible (e.g., see Fortney et al. 2007). The coefficients c_0 , c_1 and c_2 are reported in Appendix C for each value of the flattening parameter f . As shown in Fig. 3, the fit reproduces $\log R_{\text{eq}}$ with an absolute precision better than 0.003 for each compound, for any f . Clearly, c_0 exhibits the largest variations. In log. scale, the local slope β of the mass-radius relationship is deduced from Eq.(10), namely

$$\left. \frac{\partial y}{\partial x} \right|_{f=0} = c_1 + 2c_2 x \equiv \beta, \quad (11)$$

which is about 0.29 for iron and water, and 0.30 for perovskite. This is slightly lower than $\frac{1}{3}$, typical of a homogeneous body.

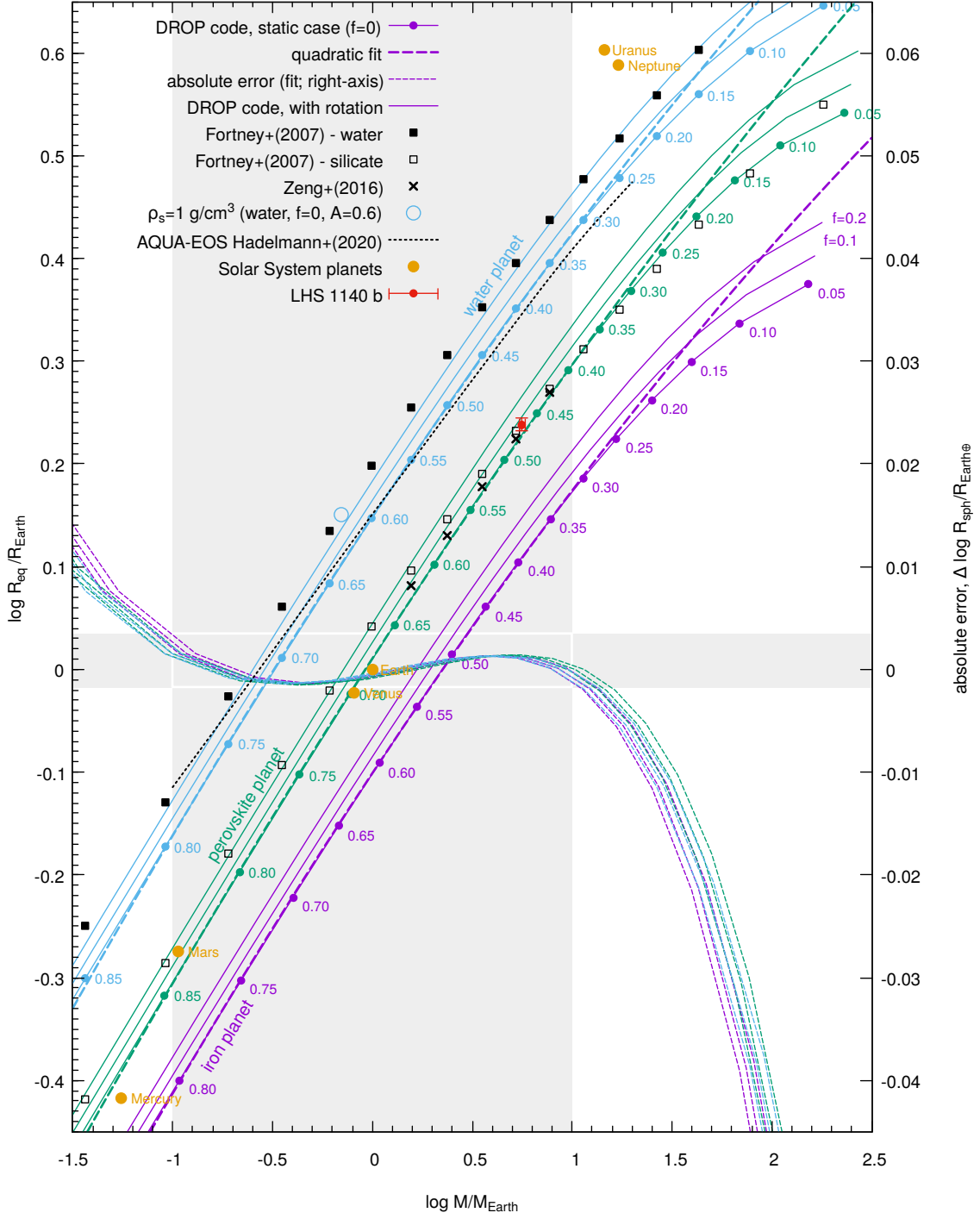


Fig. 3. Mass-radius relationships (*left axis*) computed with the DROP code in the single layer case, for iron (*purple*), perovskite (*green*), and water (*cyan*), and for three flattening parameters $f \in \{0, 0.1, 0.2\}$. Values of the input parameter A are indicated along the curves for $f = 0$; see Eq. (8). The domain where the fits are performed is indicated (*grey, shaded zone*) as well as the absolute error (*right axis*). The result obtained with $\rho_s = 1 \text{ g/cm}^3$, $f = 0$ and $A = 0.6$ for water in Eq. 4 is shown for comparison (*cyan, open circle*). Also plotted are the empirical relationship valid in the range $1 - 8 M_{\oplus}$ and built from the Earth’s model by Zeng et al. (2016) (*black crosses*), the data from Tab. B.1 of Haldemann et al. (2020) obtained from the AQUA-EOS for water assuming a 300 K surface temperature (*thin, dotted lines*), and the results by Fortney et al. (2007) for pure-water and pure-silicate planets (*open and filled squares*), all obtained in the static case. See Sect. 6 for a discussion about LHS 1140 b (*red dot*).

The leading term is coefficient c_1 , but the slope slightly decreases with increasing mass (c_2 are negative values). We see from Tabs. C.1 to C.3 that the c_i ’s depend monotonically on f . The slope β marginally increases. It happens that the c_i ’s can be very well fitted with a quadratic form in f . We therefore get a bi-quadratic

formula for the mass-radius-flattening relationship of the form

$$y \approx \sum_{i=0,2} x^i \times \sum_{j=0,2} c_{ij} f^j \equiv y(x, f), \quad (12)$$

where the c_{ij} ’s are given in the Appendix D for iron, perovskite and water planets.

3.2. Relative changes in the mass and radius due to rotation

By differentiating Eq.(12) at $f = 0$, we find

$$dy \approx \underbrace{\left(\sum_{i=0,2} c_{i1} x^i \right)}_{\text{rotation}} df + \underbrace{(c_{10} + 2c_{20}x)}_{\text{static}} dx. \quad (13)$$

It follows that, in the limit of slow rotations, the mass-radius relationship is linearly shifted upwards with respect to the static case by the quantity $\Delta R_{\text{eq}} = \eta_r f R_{\text{eq}}$ where

$$\eta_r \equiv \frac{1}{f} \frac{\Delta R_{\text{eq}}}{R_{\text{eq}}} \approx \ln 10 \times \left. \frac{\partial y}{\partial f} \right|_f \approx \ln 10 \sum_{i=0,2} c_{i1} x^i, \quad (14)$$

which depends on the mass. In the range of reference, η_r varies from 0.33 at low mass to 0.39 at high mass. For $x = y = 0$, we have

$$\eta_r \approx \ln 10 c_{01} \approx \begin{cases} 0.3611 & \text{for iron planets,} \\ 0.3551 & \text{for perovskite planets,} \\ 0.3614 & \text{for water planets,} \end{cases} \quad (15)$$

which values are close to $\frac{1}{3}$ (see Sect. I.1). We see from Tab. D.1 that c_{01} is the largest among the c_{i1} 's, whatever the material. Besides, c_{11} being positive, η_r slightly increases as the mass increases.

We can make a similar analysis at constant radius. From Eq.(13), the change in the mass is $\Delta M = \eta_m f M$ in the limit of slow rotations, with

$$\eta_m \equiv \frac{1}{f} \frac{\Delta M}{M} \approx -\ln 10 \times \left. \frac{\partial y}{\partial f} \right|_f \approx -\ln 10 \frac{\sum_{i=0,2} c_{i1} x^i}{c_{10} + 2c_{20}x}, \quad (16)$$

which depends on the mass. The mass-radius relationship is therefore shifted leftwards with respect to the static case. We see from Tab. D.1 that c_{11} and c_{21} are positive, while c_{20} is always negative. It means that $\eta_m < 0$ monotonically decreases with the mass (it varies from -1 at to about -1.5). For $x = y = 0$, we get

$$\eta_m \approx -\frac{c_{01}}{c_{10}} \ln 10 \approx \begin{cases} -1.2308 & \text{for iron planets,} \\ -1.1797 & \text{for perovskite planets,} \\ -1.2338 & \text{for water planets.} \end{cases} \quad (17)$$

3.3. Inverse formula and error bars

We can determine f as a function of M and R_{eq} from Eq.(12). If we define $\mu_j = \sum_{i=0,2} c_{ij} x^i$, then $y = \mu_0 + \mu_1 f + \mu_2 f^2$, which is easily solved for f . The root is

$$f = \frac{1}{2\mu_2} \left[-\mu_1 + \sqrt{\mu_1^2 + 4\mu_2(y - \mu_0)} \right], \quad (18)$$

which becomes $f \approx (y - \mu_0)/\mu_1$ for $f \rightarrow 0$. This is therefore the flattening required to match a given mass and radius (see Sects. 5.1 and 7.1). Any uncertainty δR_{eq} in the radius (or δM in the mass) produces an error δf in the flattening, which is also the meaning of η_r and η_m (see below).

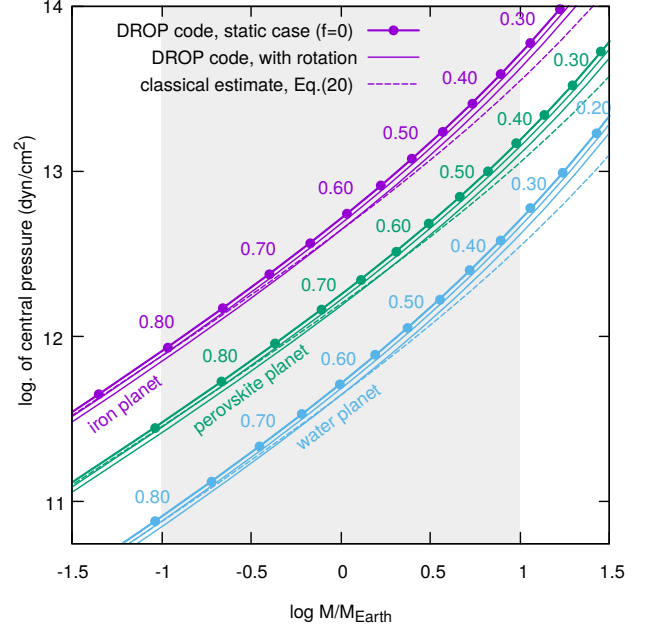


Fig. 4. The central pressure P_c in the same conditions as for Fig. 3 for $f \in \{0, 0.1, 0.2\}$, and the classical estimate P_0 for spherical systems (dashed line) according to Eq.(19).

3.4. Central pressure

The central pressure P_c is displayed in Fig. 4 in the same conditions as above, together with the classical estimate for spherical stars (Cox & Giuli 1968)

$$P_0 = \frac{3GM^2}{8\pi R_{\text{eq}}^4}, \quad (19)$$

which quantity is, in fact, a lower limit. We first notice the remarkable correlation between P_c and P_0 in the static case, which both increase with the mass. This is expected because $P_0 \propto M^{2(1-2\beta)}$, where the power-law exponent of the mass-radius relationship is, as seen before, less than $\frac{1}{2}$. For a given total mass, P_c is slightly larger in the static case than for a rotating configurations. This result, which concerns a two-layer planet with modified EOS, is therefore similar with the case of a (single-layer) polytropic gas sphere, as established in Chandrasekhar (1933a).

3.5. Rotation period

The rotation period T of the planet is displayed versus the mass in Fig. 5 for $f = 0.1$. As expected, T increases as f decreases, and is larger for smaller masses. A reliable fit can be obtained with the help of Maclaurin's formula for homogeneous spheroids, which gives the rotation rate Ω as function of the mean-mass density $\langle \rho \rangle$ and flattening f . In the limit of slow rotations, the period of the Maclaurin spheroid $T_{\text{Ml}} = 2\pi/\Omega$ is given by (e.g. Chandrasekhar 1933a)

$$T_{\text{Ml}}^2 \approx \frac{15\pi}{2G\langle \rho \rangle \left(1 - \frac{R_{\text{pol}}^2}{R_{\text{eq}}^2}\right)} \approx \frac{15\pi}{4G\langle \rho \rangle f \left(1 - \frac{f}{2}\right)}. \quad (20)$$

This formula works remarkably well with the modified EOS once the mean-mass density is known, as Fig. 5 shows, and the scaling with f is reliable. By expliciting the mean mass density,

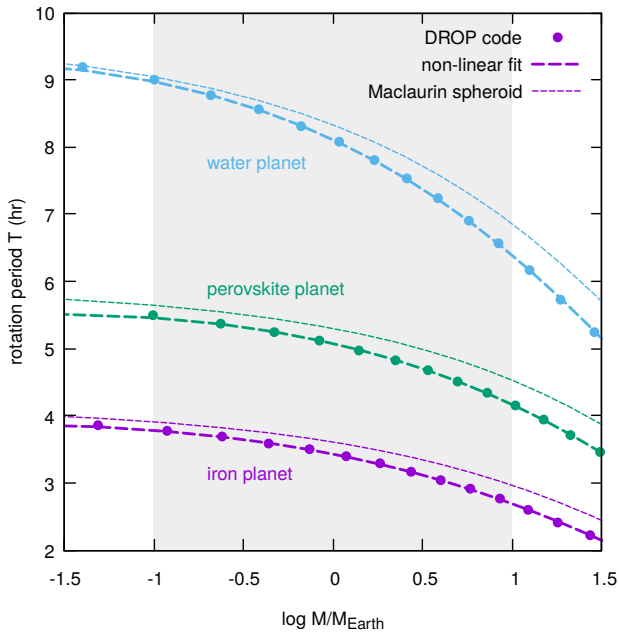


Fig. 5. The rotation period T of single-layer planets in the same conditions as for Fig. 3 for $f = 0.1$, together with the fit with Eq. (21). The period of the Maclaurin spheroid (dotted lines) having with the same flattening and same mean mass density according to Eq.(20) is also given.

we can see that the quantity $T^2 M f / R_{\text{eq}}^3$ should roughly be a constant (of the order of 0.3 in the present case). A quadratic fit in x and a linear fit in f appears sufficient, as follows

$$2 \log T - 3y + x + \log f = \sum_{i=0,2} x^i \sum_{j=0,1} t_{ij} f^j, \quad (21)$$

where the coefficients t_{ij} are given on Appendix E. The quality of the fit is visible in Fig. 5.

3.6. Note about the very-high mass part of the diagram

At very high mass, the radius goes through a maximum and then decreases with the mass. This behavior is the consequence of the bimodal EOS used here, and is fully expected (Zapolsky & Salpeter 1969; Spiegel et al. 2014). Actually, according to the theory of polytropic spheres, the mass M and radius R_{eq} are linked as follows (e.g. Horedt 2004)

$$R_{\text{eq}}^{3-n} \times M^{n-1} = \text{const.}, \quad (22)$$

and we have $\beta = \frac{1-n}{3-n}$, with the consequence that the radius remains a decreasing function of the mass (i.e. $\beta < 0$) as soon as $n > 1$, which is effective at very high pressure; see Tab. 1. The maximum occurs at about $550 M_{\oplus}$ for iron and silicate and much beyond for water. It is therefore not visible in the figure, and out of the range of interest here.

4. Results for two-layer planets

We have run the code with $\mathcal{L} = 2$ for the same parameters A and f as above, and with $q \in \{0.1, 0.2, \dots, 0.9\}$. The mass-radius relationships obtained for CE=IW in the static case are displayed in Fig. 6 as a function of q for a given A (hereafter, a q -sequence), and as a function of A for a given q (hereafter, a A -sequence). A sub-figure shows the effect of rotation for $f = 0.2$. The data

obtained for $f = 0.1$ and $q = 0.5$, which corresponds to Saturn's oblateness, are gathered in Tab. A.1 (bottom). We see that the mass-radius relationship stands between the two curves obtained in the single-layer cases $C=\{I,W\}$, and we have similar trends as for single-layer cases (i.e. the radius increases as f increases). The A -sequences are roughly linear in the domain of interest, parallel to each other, but with a marked curvature at high mass. All q -sequences are also roughly parallel to each other but are non-bijective, for any A . As q increases, the mass and radius first decrease until $q \approx 0.6$, then the variation is fully reversed. The results obtained for iron/perovskite and for perovskite/water are displayed in Figs. F.1 and G.1, respectively. We make similar observations as for the IW planet. The diagrams are a little bit more compact because $\rho_s(C)/\rho_s(E)$ is smaller than for the IW case.

4.1. Fitting procedure

Whatever the mineralogical composition, we can fit the data in the reference mass range (see Sec. 3) by a quadratic law, i.e. with Eq.(10). The process is a little bit more complex than for the single-layer case, because there is an additional parameter. The coefficients obtained for each A -sequence where q and f are held fixed are now denoted c'_i , with $i = \{0, 1, 2\}$. These are listed in Tab. H.1 for the static IW-planet, together with mean values $\langle c'_i \rangle$ and half-amplitudes of variation Δ_i defined by

$$\begin{cases} \langle c'_i \rangle = \frac{1}{9} \sum_q c'_i, \\ 2\Delta_i \equiv \max\{c'_i\} - \min\{c'_i\}, \end{cases} \quad (23)$$

where the single-layer data are excluded. This procedure is repeated for each value of the flattening parameter.

4.1.1. A sigmoid for the coefficient c'_0

We find that c'_0 exhibits marked variations with the core size. It is plotted versus q in the IW-case in Fig. 7 for all the flattening parameters considered, including the static case. In fact, $c'_0(q)$ can be approximated by a smooth function, but a quadratic law is not really appropriate. A better choice is a symmetrical sigmoid, namely

$$c'_0(q) = \frac{d_0 + d_1 q^\sigma}{1 + d_2 q^\sigma}, \quad (24)$$

where the coefficient $d_0 = y(0)$ corresponds in principle to the single layer case; see the coefficients c_{0j} in Tabs. C.1 to C.3. The analysis reveals that d_0 , d_1 , d_2 and the exponent σ vary very weakly with f , and can all be fitted by a parabola. However, for Eq.(24) to be easily/analytically reversible in the variable f , we deliberately use a unique value for σ regardless of the flattening parameter f . We then decide to use the value obtained in the static case, namely $\sigma \approx +2.7$. The parameters d_0 , d_1 and d_2 of the sigmoidal fit are given in Tab. H.2 for the IW-planet. It happens that these quantities vary monotonically with f , and can be very well approximated by a parabola, again, i.e. $d_i = \sum_{j=0,2} d_{ij} f^j$. The coefficients d_{ij} of these three fits are listed in Tab. I.1 for CE= $\{IW,IP,PW\}$. Figure 7 also displays the absolute error in fitting c'_0 by Eq. (24), which turns out to be less than about 0.001 for $q \leq 0.9$ and $f \leq 0.2$. We get a similar magnitude for the IP and PW-cases.

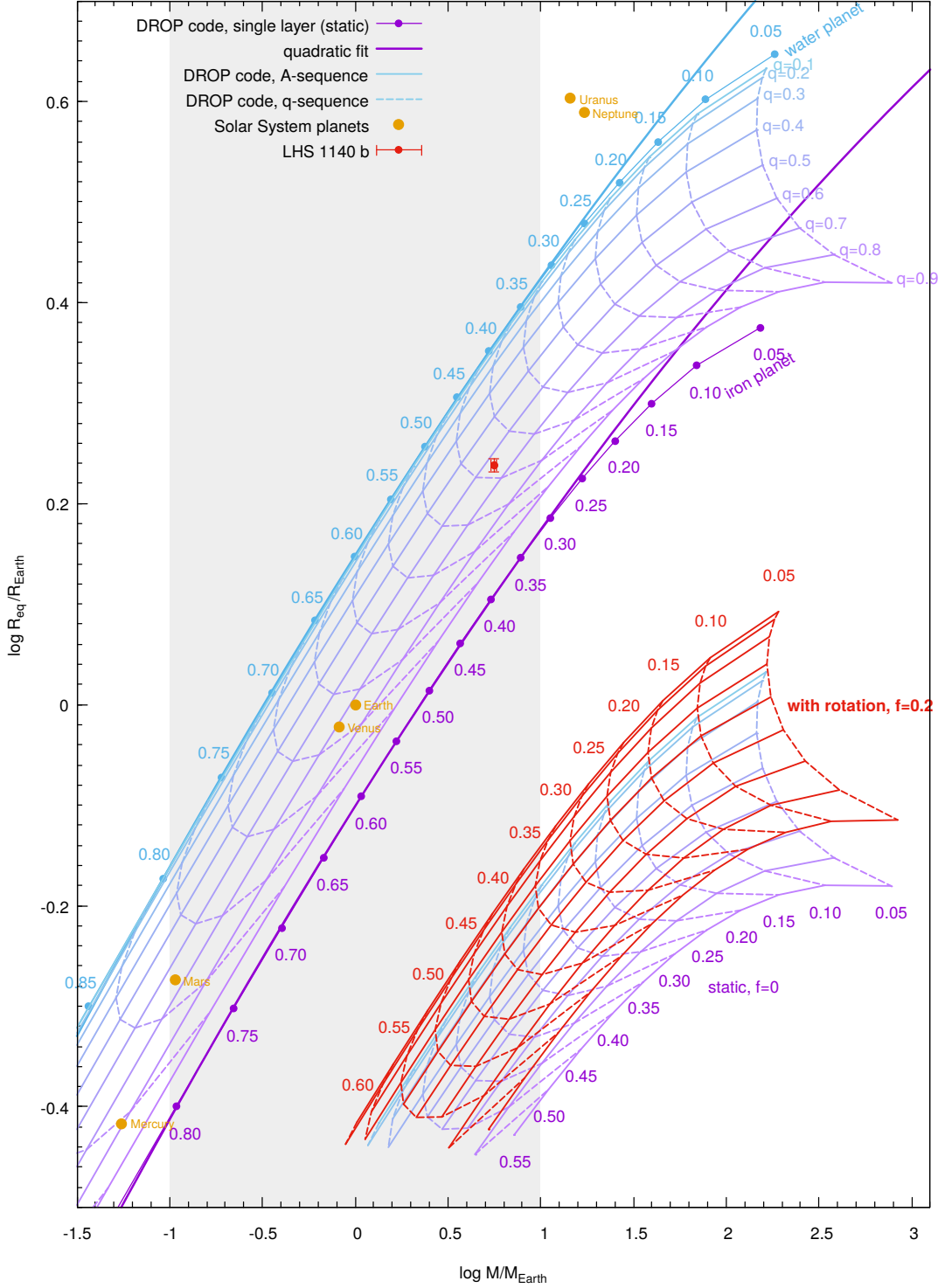


Fig. 6. Same caption as for Fig. 3 but in a two-layer IW-planet, in the static case. Labels refer to values of top-to-bottom mass density ratio A (single-layer), and the relative size of the core q along the sequences. The effect of rotation is also shown for $f = 0.2$ (bottom right, red lines; a vertical shift of -0.6 applied for clarity).

4.1.2. A parabola for the next two, averaged coefficients

Figure I.1 shows the mean values $\langle c'_1 \rangle$ and $\langle c'_2 \rangle$ and the associated deviations Δ_i defined by Eq. (23) versus f , still in the IW-case. We see that, in contrast with c'_0 , the coefficients c'_1 and c'_2 do not vary much with the core size q . The size of the error bars is about 0.002 at most for c'_1 and about 0.003 for c'_2 , in absolute. As c'_2 is lower than c'_1 by a factor 10 for any $f \leq 0.2$, working with mean

values introduces an absolute error in y of the order of 0.002, mainly caused by the substitution $c'_1 \rightarrow \langle c'_1 \rangle$. As $|x| \leq 1$ for the reference mass range, the impact is an error of the order of 0.002 in y . Next, we use a parabola to fit $\langle c'_1 \rangle$, i.e.

$$\langle c'_1 \rangle = \sum_{j=0,2} c'_{1j} f^j, \quad (25)$$

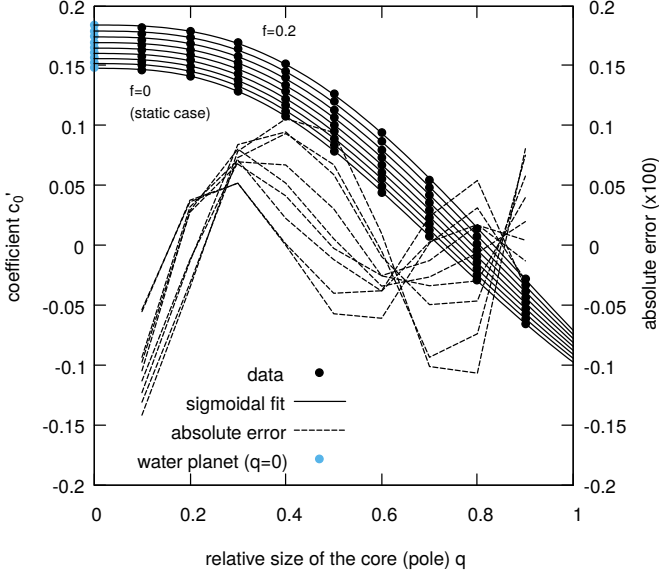


Fig. 7. Coefficient c'_0 obtained in the IW-case fitting the mass-radius relationship for a given value of the core fractional size q , for each flattening parameter f (dots). The fits by a sigmoid are superimposed (plain lines), and the absolute error is also shown (dashes lines, right axis).

while a linear function appears sufficient for $\langle c'_2 \rangle$. The coefficients c'_{1j} and c'_{2j} are listed in Tab. I.1 of the Appendix for the three types of composition. The quality of these two fits is visible in Fig. I.1 (right axis) for CE=IW. As the absolute error is less than 10^{-4} , the error is dominated by the averaging procedure, i.e. 0.002 in absolute, and not by the fit of mean coefficients.

4.2. The parametric mass-radius relationship

It follows that we get a complete parametric expression of the mass-radius relationship for two-layer planets, namely

$$y \approx \underbrace{\frac{d_0 + d_1 q^\sigma}{1 + d_2 q^\sigma}}_{\text{coefficient } c'_0} + \langle c'_1 \rangle x + \langle c'_2 \rangle x^2 \equiv y(x, q, f). \quad (26)$$

The fractional size of the core q is uniquely contained in the first term, while the effect of rotation is hidden in all the coefficients. Given the discussion above, the absolute error in fitting y is estimated to

$$\Delta y \approx \underbrace{\Delta c'_0}_{0.01} + \underbrace{\Delta \langle c'_1 \rangle}_{0.002} |x| + \underbrace{\Delta \langle c'_2 \rangle}_{0.003} |x|^2 \lesssim 0.015, \quad (27)$$

which corresponds, at most, to a relative error of 1.5% in the radius for the whole reference mass range. Depending on the application and context, Eq.(26) can be adapted or degraded, for instance by omitting quadratic terms in x and/or f . The advantage of this formula is that it is easily invertible in any of the two variables M and q (see below). We can test Eq.(26), for instance in the IP-case, by setting $M = 1 M_\oplus$ (i.e. $x = 0$), $q = 0.5$ and $f = 0.05$, which corresponds to the example of Fig. 2. The formula gives $y \approx -0.00196$, leading to $R_{\text{eq}} \approx 0.99551 R_\oplus$. This is in excellent agreement with the value determined by the DROP code and reported in Tab. 2.

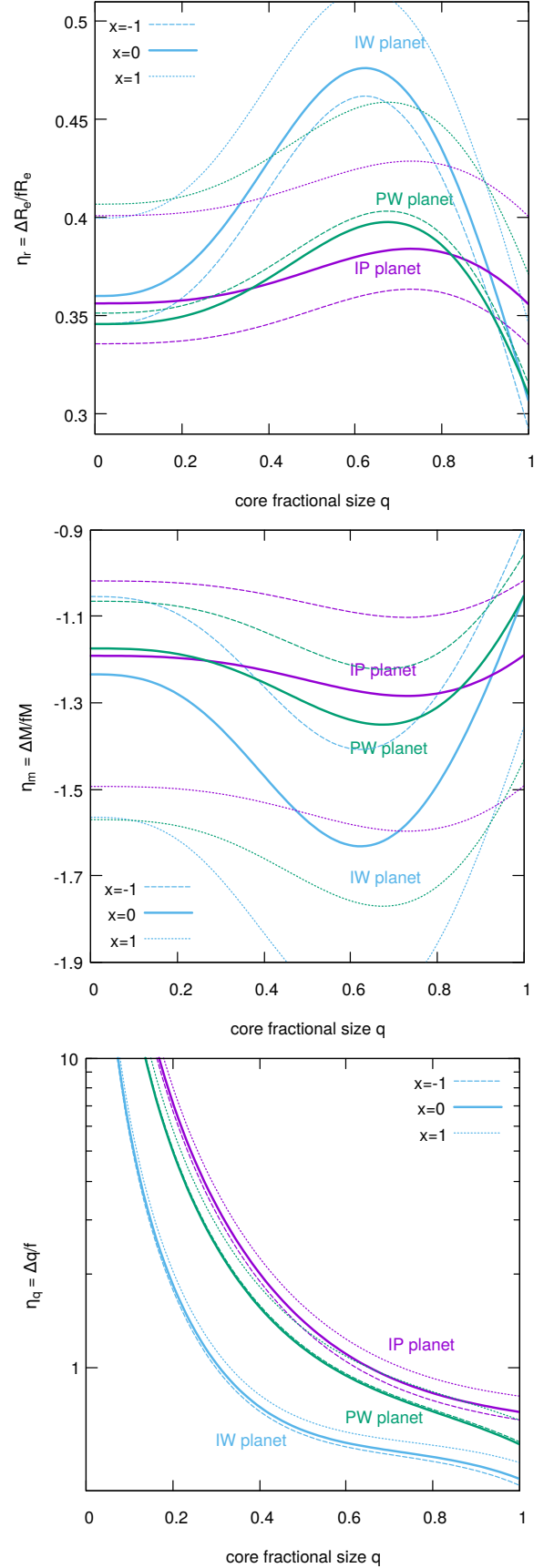


Fig. 8. Parameters η_r (top), η_m (bottom) and η_q (bottom) measuring the relative change in the equatorial radius, mass and core fraction respectively with rotation (in units of f) as a function of the core size q for $0.1 M_\oplus$, $1 M_\oplus$ and $10 M_\oplus$.

4.3. Effect of rotation detailed

As done for the single-layer case, we can differentiate Eq.(26) in the vicinity of $f = 0$. The partial derivatives are

$$\left. \frac{\partial y}{\partial x} \right|_{q,f} \approx c'_{10} + 2c'_{20}x \equiv \beta, \quad (28)$$

and

$$\left. \frac{\partial y}{\partial f} \right|_{q,f} \approx \left[\frac{d_{01} + d_{11}q^\sigma}{1 + d_{20}q^\sigma} - \frac{(d_{00} + d_{10}q^\sigma)d_{21}q^\sigma}{(1 + d_{20}q^\sigma)^2} \right] + c'_{11}x + c'_{21}x^2, \quad (29)$$

and these depend on the mass and especially on the fractional size. Note that the power-law index β of the mass-radius relationship is given by $\langle c'_1 \rangle$, which is mainly represented by the coefficient c'_{10} . This coefficient is close to 0.3, as in the single-layer case. We can then deduce η_r by varying the radius at constant mass, and η_m by varying the mass at constant radius, namely

$$\eta_r = \ln 10 \times \left. \frac{\partial y}{\partial f} \right|_{q,f}, \quad (30)$$

and

$$\eta_m = -\ln 10 \times \frac{\left. \frac{\partial y}{\partial f} \right|_{q,f}}{\left. \frac{\partial y}{\partial x} \right|_{q,f}}. \quad (31)$$

Figure 8 show η_r and η_m versus q for the three types of compositions. We notice that response to rotation goes through an extremum, which is fully calculable from Eq.(29). In the static case, the extremum stands at $q \approx 0.62$ for an IW-planet, which corresponds to a core mass fraction of 0.65 from Fig. 9. This is $q \approx 0.73$ and $M_1/M \approx 0.60$ for the IP-planet, and $q \approx 0.67$, and $M_1/M \approx 0.56$ for the PW-planet.

We can continue this analysis by considering the third derivative $\partial y / \partial q$, and define

$$\eta_q = \frac{1}{f} \Delta q \approx -\frac{\left. \frac{\partial y}{\partial f} \right|_{x,y}}{\left. \frac{\partial y}{\partial q} \right|_{x,y}}, \quad (32)$$

which gives the link between f and q keeping simultaneously the mass and the radius of the planet fixed. For instance, a PW-configuration with $f = 0$ and $q = 0.5$ has the same mass and same radius as another PW-configuration with $f = 0.1$ and $q = 0.5 + 0.1 \times 1.16 \approx 0.616$ (since we get $\eta_q \approx 1.16$ from the graph). This formula must, however, be manipulated with caution because f is intended to be much smaller than unity as well as Δq . Figure 8 shows η_q versus q . As expected from Figs. 6, F.1 and G.1, the changes are relatively small for core sizes larger than about 0.6, and very large at small q .

4.4. Core/envelope discrimination

Following the fitting procedure, q appears only in the sigmoidal representation of coefficient c'_0 . As a consequence, we can express the relative size of the core as function of the mass, radius and flattening parameter f . From Eq.(26), we find

$$q = \left[\frac{y - c'_1 x - c'_2 x^2 - d_0}{d_1 - d_2 (y - c'_1 x - c'_2 x^2)} \right]^{\frac{1}{\sigma}} \equiv q(x, y, f), \quad (33)$$

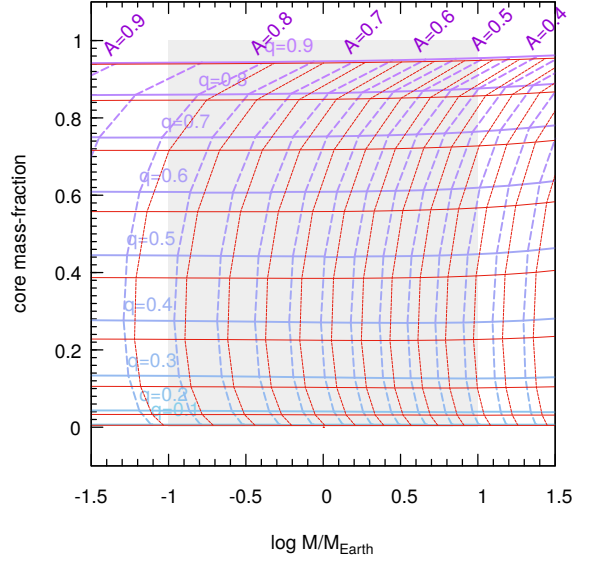


Fig. 9. Core mass-fraction versus the mass for the IW planet in the static case (*color gradient*) and for $f = 0.2$ (*red*); see the Appendix J for the IP and PW-planets.

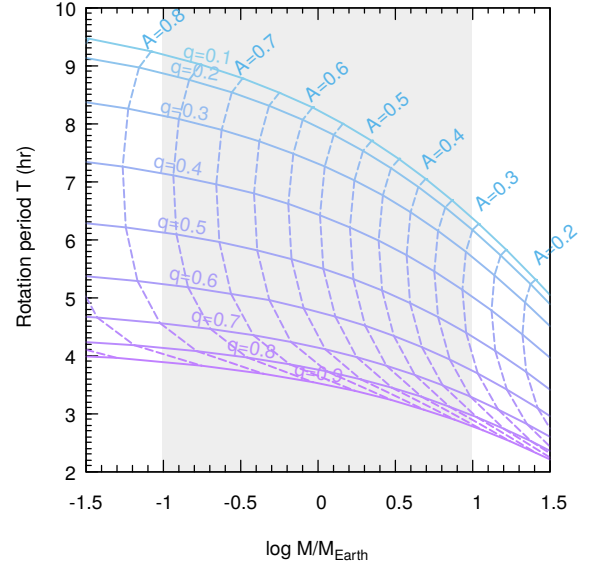


Fig. 10. Same caption as for Fig. 9, but for the period T computed for $f = 0.1$; see the Appendix J for the IP and PW-planets.

which assumes that the term inside the brackets is positive (and less than unity). It is of particular interest because it gives a first estimate of the relative size of the core for a given mass and radius (Brinkman et al. 2024). This avoids a full scan of the parameter space. Note that any uncertainty in the radius and/or mass induces an error δq in the fractional core size q (see Sect. 5).

$$\begin{aligned} \text{mass}=1.; \text{dmass}=0.1; \text{radius}=1.3; \text{dradius}=0.13 \\ \text{mass}=1; \text{dmass}=0.1; \text{radius}=0.85; \text{dradius}=0.085 \end{aligned}$$

4.5. Core mass fraction and rotation period

The core mass-fraction M_1/M is unfortunately not an input in the simulations, but an output. It is shown in Fig. 9 for the IW configurations, and for $f \in \{0, 0.2\}$; the figures obtained in the IP and PW-cases are reported in the Appendix J. We see that

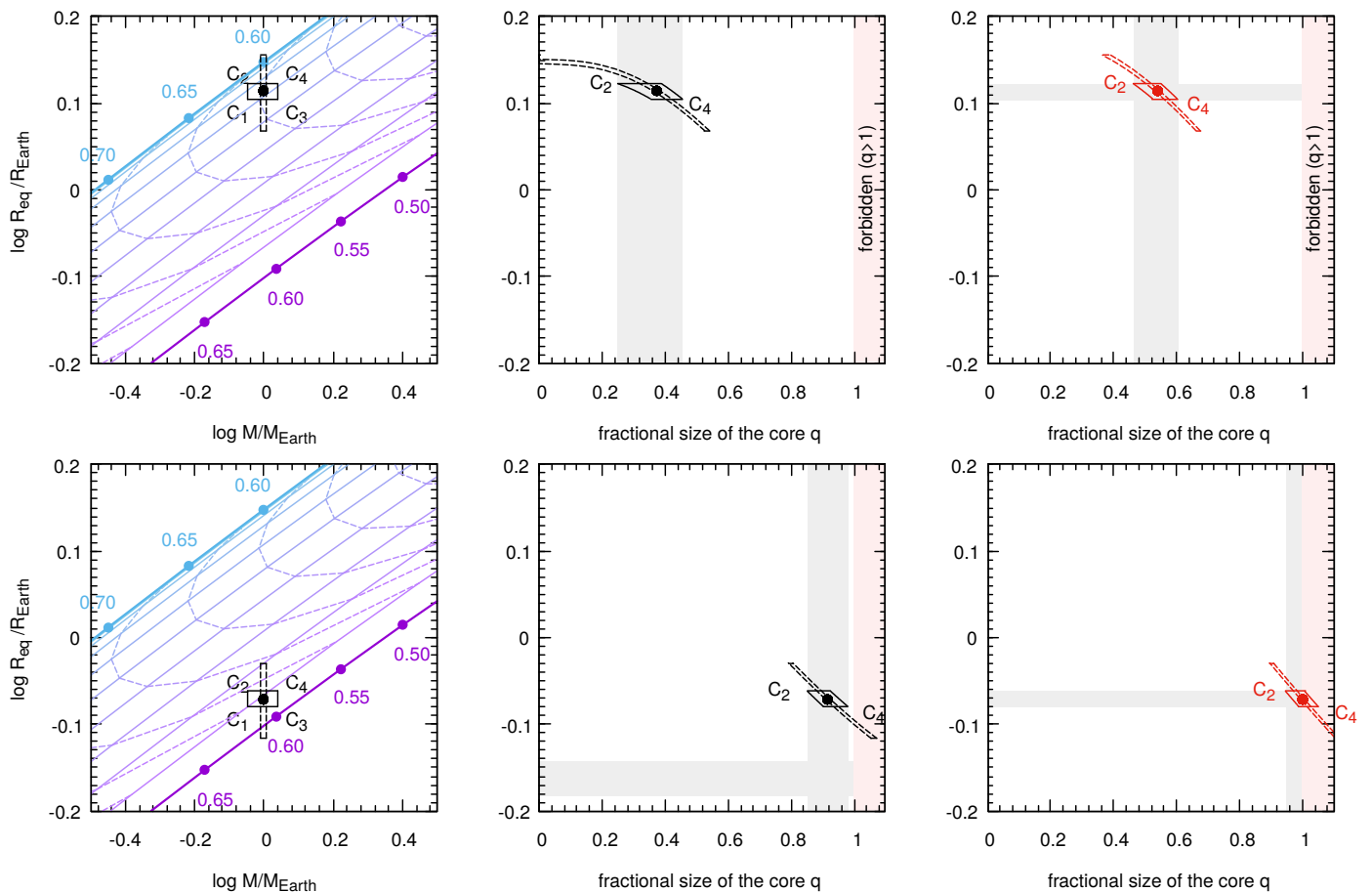


Fig. 11. Four sets of fiducial data ($M \pm \delta M, R_{\text{eq}} \pm \delta R_{\text{eq}}$) placed in the mass-radius relationship for IW-planets (*left panels*) for $M = 1 M_{\oplus}$, and $R_{\text{eq}} = 1.3 R_{\oplus}$ (*top*) and $R_{\text{eq}} = 0.85 R_{\oplus}$ (*bottom*). Error bars are $\delta M/M = 0.1$ and $\delta R_{\text{eq}}/R_{\text{eq}} = 0.02$ (*black, plain lines*) and $\delta M/M = 0.02$ and $\delta R_{\text{eq}}/R_{\text{eq}} = 0.1$ (*black, dotted lines*). The image of the error bars in terms of fractional size q is shown in the static case (*middle panels*) and with fast rotation $f = 0.2$ (*right panels*). See also Fig. 6.

the core mass-fraction is very well correlated with the core size q . This is true whatever the rotation state of the planet. The effect of rotation is weak. For a given total mass and fractional size of the core q , the core mass-fraction is the largest when the planet is static, and it decreases with rotation. Figure 10 shows the rotation period T versus the mass for $f = 0.1$. As for the single-layer case, the scaling with f given by Eq. (20) is reliable. The rotation period decreases with increasing mass, which is the consequence of the rise of the mean mass density $\langle \rho \rangle$ with M . As we have $R_{\text{eq}}(\text{IW}) > R_{\text{eq}}(\text{IP})R_{\text{eq}}(\text{PW})$ for a given mass, T is the largest for IW-planet, and the lowest in the PW-case.

5. Error bars

Positioning a planet, in precomputed mass-radius relationships for single layers enables to determine how far/close to a pure composition the body is, and therefore to deduce plausible combinations of compositions, either in the form of a mixture of materials or in the form of distinct layers (see below). In terms of number of layers, composition and rotational state, the level of degeneracy depends not only in the position but also on the size of error bars on the radius δR_{eq} and on the mass δM .

5.1. Single-layer models

As shown in Sect. 3, including rotation moves the mass-radius relationship upwards (i.e. towards larger radii). So, if observational error bars permit, a position in the diagram can be interpreted in terms of a deviation to a pure composition or in terms of rotation, or both. This can easily be checked by running the DROP code by selecting all values of f that lead to a given pair ($M \pm \delta M, R_{\text{eq}} \pm \delta R_{\text{eq}}$), but a scan of the parameter space is costly. The advantage of the simulation is that we can impose high values of f , up to the break-up velocity. In the theory of ellipsoidal figures of equilibrium Chandrasekhar (1969), the homogeneous spheroids in rigid rotation are stable for values of the flattening parameter up to $f \approx 0.42$, which corresponds to the transition towards states of lower energies in the form of triaxial bodies. However, if $f \leq 0.2$, we can use Eq.(18) as an approximation, and we can include the corresponding error bars δx and δy , and even use the η_m and η_r parameters for small f values. An illustration is given in Sect. 6.

5.2. Two-layer models

With two-layer diagrams, the degeneracy increases and the interpretation is less clear. For instance, we see from Figs. 6, F.1 and G.1 that the data $(x, y) = (1, 0.3)$ is compatible with static IW, IP and PW-planets, differing by the size of their core. Again, in the spherical case, we can scan the region in the diagram nu-

merically with the DROP and select the right pairs (q, A) on input compatible with error bars. We then get a range δq of fractional sizes as the image of $(x_0 \pm \delta R_{\text{eq}}, y_0 \pm \delta M)$. As shown, rotation represents another degree of freedom (and a source of confusion in the inverse problem). We can therefore repeat this treatment by varying f , and it follows that δq becomes a function of f . In fact, we can directly access the image of error bars in terms of q and f by using Eq. (33).

As an illustration, we show in Fig. 11 two positions $(x_0 \pm \delta x, y_0 \pm \delta y)$ in the IW diagram, and the image of error bars in terms of core size q obtained from Eq.(33) in the static case $f = 0$ and for $f = 0.2$. The extreme points C_i obtained by considering $\pm \delta x$ and $\pm \delta y$ are also reported. We see that:

- the image of the error bar in the radius $R_{\text{eq}} \pm \delta R_{\text{eq}}$ is an error bar in the core size around q_0 ,
- the image of the error bar in the mass $M \pm \delta M$ is another error bar in the core size around q_0 ,
- the two error bars in the core size are not equal, not symmetrical around q_0 , non-linear in δR_{eq} and δM , and sensitive to rotation.

Error bars in terms of fractional size. We see from the figures that $q \in [q_{\text{min}}, q_{\text{max}}]$, where the lower and upper bounds correspond to points $C_2(x_0 - \delta x, y_0 + \delta y)$ and $C_4(x_0 + \delta x, y_0 - \delta y)$, respectively. We can therefore retain

$$\begin{cases} q_{\text{min}} \equiv q(x_0 - \delta x, y_0 + \delta y, f), \\ q_{\text{max}} \equiv q(x_0 + \delta x, y_0 - \delta y, f), \end{cases} \quad (34)$$

where $\delta x > 0$ and $\delta y > 0$. Note that q_{min} and q_{max} are not symmetrical with respect to $q_0 = q(x_0, y_0, f)$, unless the uncertainties are small. In these conditions, we have

$$(x_0 - \delta x, y_0 + \delta y) \rightarrow 2\delta q \approx q_{\text{max}} - q_{\text{min}} \quad (35)$$

in the general case. In the limit of small uncertainties, we can deduce an expression for δq by differentiation of Eq.(33). This approach uses the derivatives established in Sect. 4.3.

Error bars in terms of flattening. The flattening parameters compatible with a given observational data can be estimated from η_r and η_m , by using Eqs. (30) and (31) where ΔR_{eq} and ΔM are to be replaced by δR_{eq} and δM , respectively. Assuming that the spherical configuration $f = 0$ is reachable by the model and q is fixed, we have

$$\delta f \approx \max\left(\frac{1}{\eta_r} \frac{\delta R_{\text{eq}}}{R_{\text{eq}}}, -\frac{1}{\eta_m} \frac{\delta M}{M}\right), \quad (36)$$

which differs from one composition to another. So, for a given fractional size q , we have

$$(x_0 - \delta x, y_0 + \delta y) \rightarrow \delta f \quad (37)$$

where δf can be directly read from Fig. 8.

6. Illustration with the parameters of LHS 1140 b

For a suitable application, we searched for a transiting super-Earth with a confirmed status and a good precision on the mass and on the radius. We have selected the targets from the Nasa Exoplanet Archive (Akeson et al. 2013) and European exoplanet database with a maximum radius of $1.8R_{\oplus}$. From the semi-major axis a and mass M_{\star} of the host star, the candidates have then been ordered with increasing parameter a^6/M_{\star}^2 which scales

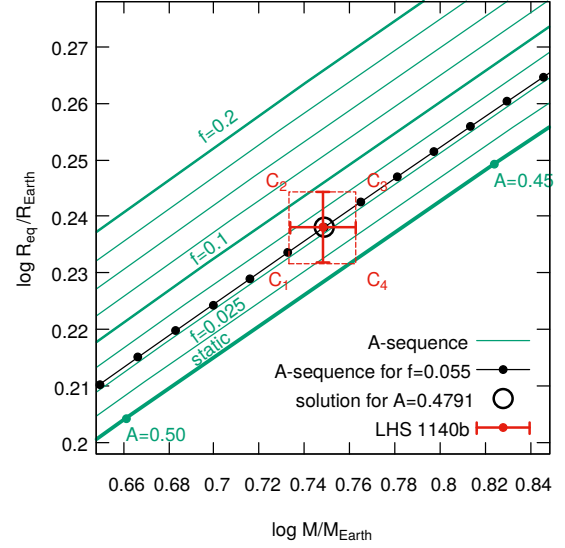


Fig. 12. Position of LHS 1140 b (red) in the mass-radius diagrams for single-layer, pure-perovskite planets obtained for different flattening parameters. The A-sequence obtained with the DROP code for $f = 0.055$ is also plotted (black); see Fig. 3.

with their tidal locking time (Zahn 1989; Leconte et al. 2015; Barnes 2017). Unfortunately, all robust super-Earth candidates with a radius measurement currently discovered are expected tidally locked, because of their short orbital periods and presumed age. The comparison with our models can therefore not account for the final spin state of the planet, and therefore remains purely illustrative. We have selected LHS 1140 b, which represents a fair trade off, because it exhibits among the largest synchronisation time scale. This planet has been detected by both photometric transit and radial-velocity measurements by different groups (Dittmann et al. 2017; Ment et al. 2019; Lillo-Box et al. 2020; Cadieux et al. 2024a). It orbits a M-dwarf star located at about 12 pc away from the Sun. It has an averaged mass-density compatible with an iron/silicate content. In addition, the installation conditions seem to permit water, if present, to be in liquid phase, making this object of particular interest in several respects (Wandel 2018). This planet has recently been modelled by Rigby & Madhusudhan (2024) and Daspute et al. (2024), with up to four differentiated layers (including a thin atmosphere). The water layer could be 2000 km deep, and the ocean might represent up to 7% of it in the nominal cases. The internal structure of LHS 1140 b is still under debate. It is commonly interpreted either as water world or a mini-Neptune, but the recent spectroscopic observation with JWST disfavor a body with dihydrogen- and methane-rich atmosphere, hence the second option (Cadieux et al. 2024b).

In this section, we use $R_{\text{sph}} = 1.730 \pm 0.025 R_{\oplus}$ as the spherical radius and the mass is $M = 5.60 \pm 0.19 M_{\oplus}$, according to Cadieux et al. (2024a). In decimal logarithm, these data correspond to $x_0 \pm \delta x \approx 0.7482^{+0.0145}_{-0.0150}$ and $y_0 \pm \delta y \approx 0.2380^{+0.0062}_{-0.0063}$. In the absence of any information about the orientation of the rotation axis with respect to the line of sight, we assume $R_{\text{sph}} = R_{\text{eq}}$ for simplicity. This setting is correct only in the case of a circular transit, i.e. the planet is exceptionally seen pole-on. We can then directly place the planet in the mass-radius diagrams, without any bias. Otherwise, a correction must be applied (see Sect. 7.4).

Table 3. Flattening from Eq.(18) and rotation period from Eq.(21) for the parameters of LHS 1140 b assuming a pure perovskite planet, compared to the Earth.

| point | x | y | flattening f | period T |
|--------------|---------|---------|----------------|------------|
| (x_0, y_0) | 0.74822 | 0.23804 | 0.0636 | 5.51 |
| C_2 | 0.73320 | 0.24428 | 0.1204 | 4.08 |
| C_4 | 0.76268 | 0.23172 | 0.0026 | 26.78 |
| Earth | 0 | 0 | 0.0034 | 24 |

6.1. Single-layer models

We see from Fig. 3 that a pure water planet is not possible, and that the iron hypothesis is not sustainable, unless a very large rotation rate is invoked. Actually, as shown before, the mass-radius relationships are shifted upwards when $f > 0$, and the faster the rotation, the larger the shift. The only plausible solution is obtained with perovskite, but some rotation is necessary. According to the figure, $f < 0.1$ at a one sigma confidence level. A zoom is presented in Fig. 12. By using the DROP-code, we find $f = 0.055$ for the central value of the observational interval, while we get $f \approx 0.064$ from the fit by Eq.(18). The deviation between these two values is due to the quality of the fit. By considering errors bars and especially points C_2 and C_4 (see Sect. 5), we get the values of Tab. 3, where the associated rotation period is also reported.

6.2. Two-layer models

Figure 13 shows the position of the planet in the mass-radius diagrams for an IW-, an IP- and a PW-planet, together with the error bars through the points C_i 's. We can feed Eq.(26) with the observational data, and in particular with the error bars, as done in the single-layer case. The results obtained for three rotational states are gathered in Tab. 4. In the static case, LHS 1140 b is compatible with an iron core/water envelope planet for $q \approx 0.64 \pm 0.03$, and with a perovskite core/water envelope planet for $q \approx 0.94 \pm 0.04$, while the IP solution is ruled out. New solutions are permitted with rotation. While we can consider relatively large values for f , it is interesting to use Eq.(36) to get the range of rotation states compatible with the error bars. For LHS 1140 b, we have $\delta R_{\text{sph}}/R_{\text{sph}} \approx 0.01445$, and $\delta M/M \approx 0.03393$. As a consequence, from the fractional size obtained in the spherical case, we find for the range of flattening parameters compatible with the error bars

- $\delta f \approx 0.029$ for the IW-planet,
- $\delta f \approx 0.038$ for the PW-planet,

and the corresponding period is $T \approx 7.5$ h in both cases.

The IW hypothesis. If rotation is accounted for, type IW solutions remains fully available. The iron core is larger and more massive. By using the DROP code, we can scan the parameter space and extract the structures compatible with the observational data. In this task, Eq.(33) is of great help as the right range of fractional sizes q is fastly identified. Figure 14 shows the fractional size q , the parameter A , the core mass fraction M_1/M , the central pressure P_c , an estimate of the ocean depth (see Sect. 7.3) and the rotation period T obtained for $f \in \{0, 0.1, 0.2\}$. We see that the range of fractional sizes as given by Eq.(33) is in very good agreement with the numerical approach. We find $q \approx 0.635 \pm 0.025$, and the core-mass fraction is 0.66 ± 0.04 in the non-rotating case. These ranges are

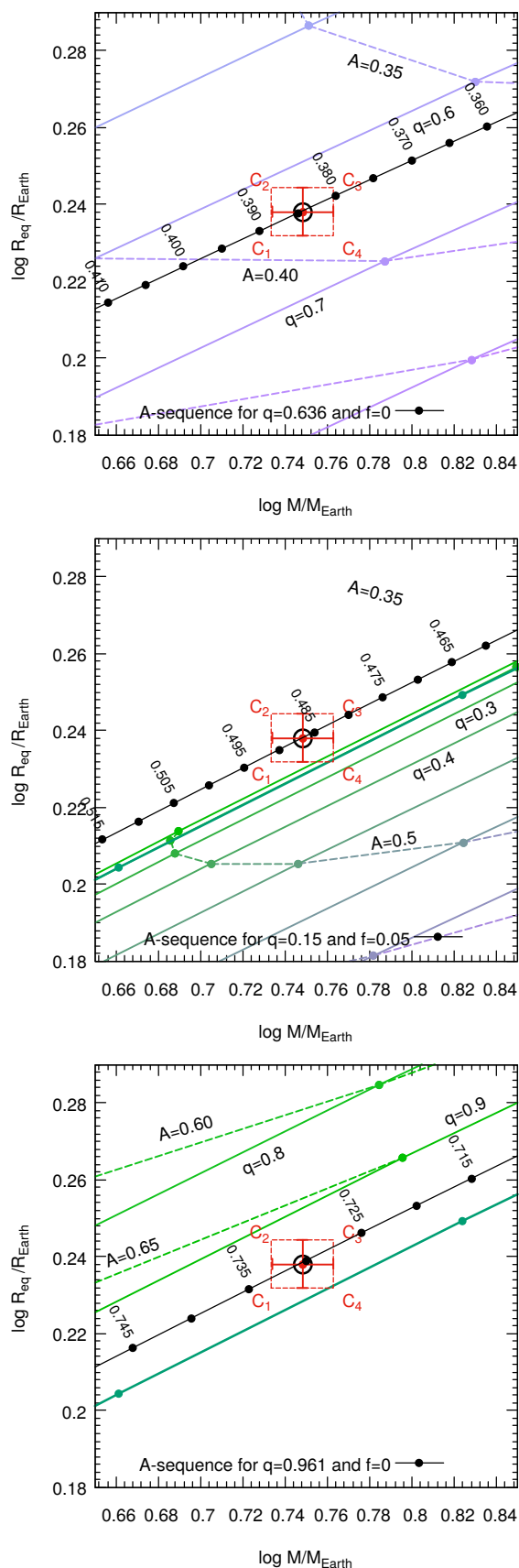


Fig. 13. Position of LHS 1140 b (red) in the mass-radius diagram for IW-planets (top panel), for IP-planets (middle panel) and for PW-planets (bottom panel). The one-sigma error bars are taken from (Cadieux et al. 2024a). The best static A-sequence is also plotted for IW- and PW-configurations (black); see also Fig. 15 and Tab. 5.

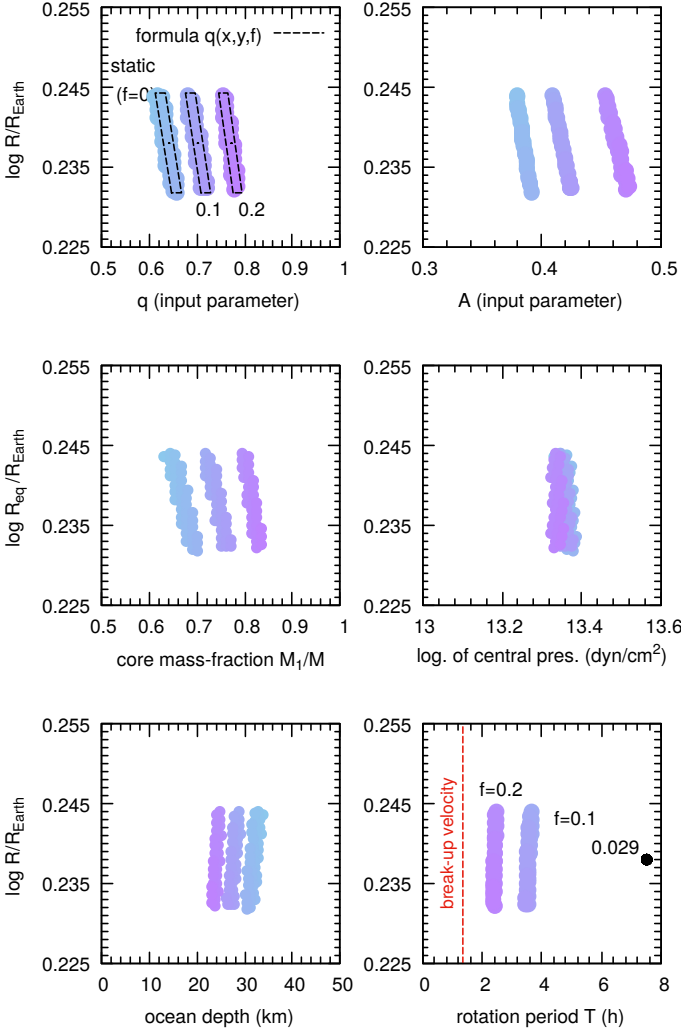


Fig. 14. Structure parameters of LHS 1140 b compatible with the error bars (see Fig. 13, top panel) computed with the DROP code, assuming a two-layer, IW-planet in three rotational states. The color code refers to values of the core fractional size, which is smaller in the static case than with rotation; see also Fig. 6. Regarding the ocean depth, see Sect. 7.3. As an indication of the break-up velocity (which depends on q), we have reported in the last panel the Keplerian period at the planet equator (red) as well as the period associated to $\delta f = 0.029$, which amplitude corresponds to the error bars in the static case; see Eq. (36).

pushed towards higher values with rotation. The ocean-depth is estimated to be at least about 30 km, and it decreases as f increases. The rotation period, which roughly varies like $1/\sqrt{f}$, is already as low as about 4 h for $f = 0.1$.

The IP hypothesis. As Tab. 4 shows, an iron core/perovskite envelope planet is a plausible option for LHS 1140 b, but this requires some rotation, again. The core has a small size and a low mass in relative. For $f = 0.1$ for instance, we have $q \approx 0.33^{+0.13}_{-0.04}$. We have plotted in Fig. 13 (middle panel) the A -sequence obtained with the DROP-code for $f = 0.05$ and $q = 0.15$. The solution obtained for $A \approx 0.4866$ matches the central value (x_0, y_0) very well. Output data are gathered in Tab. 5 and the pressure and mass-density maps are displayed in Fig. 15. In this simulation, the iron core is less than 1% of the planet’s mass, the rotation period is 6 h 24 min.

Table 4. Relative core size q calculated from Eq.(33) for LHS 1140 b in different spin states $f \in \{0, 0.1, 0.2\}$, assuming a two-layer planet.

| | f | (x_0, y_0) | C_1 | C_2 | C_3 | C_4 |
|----|---------------------|----------------|----------------|----------------|----------------|-------------------------|
| IW | 0 | 0.641 | 0.647 | 0.613 | 0.634 | 0.668 |
| | 0.10 | 0.703 | 0.708 | 0.676 | 0.696 | 0.729 |
| | 0.20 | 0.771 | 0.776 | 0.746 | 0.765 | 0.795 |
| IP | 0 | $q^\sigma < 0$ | $q^\sigma < 0$ | $q^\sigma < 0$ | $q^\sigma < 0$ | $q^\sigma < 0^\ddagger$ |
| | 0.0681* | 0 | | | | |
| | 0.0636 [†] | 0 | | | | |
| | 0.10 | 0.3277 | 0.364 | $q^\sigma < 0$ | 0.280 | 0.466 |
| | 0.20 | 0.5638 | 0.580 | 0.470 | 0.547 | 0.637 |
| PW | 0 | 0.937 | 0.946 | 0.894 | 0.927 | 0.979 |
| | 0.0962* | 1 | | | | |
| | 0.10 | $q^\sigma > 1$ | $q^\sigma > 1$ | 0.964 | 0.994 | $q^\sigma > 1$ |
| | 0.20 | $q^\sigma > 1$ |

*single-layer limit of Eq.(33)

[†]from Eq. (18)

[‡]tiny core solution with the DROP code

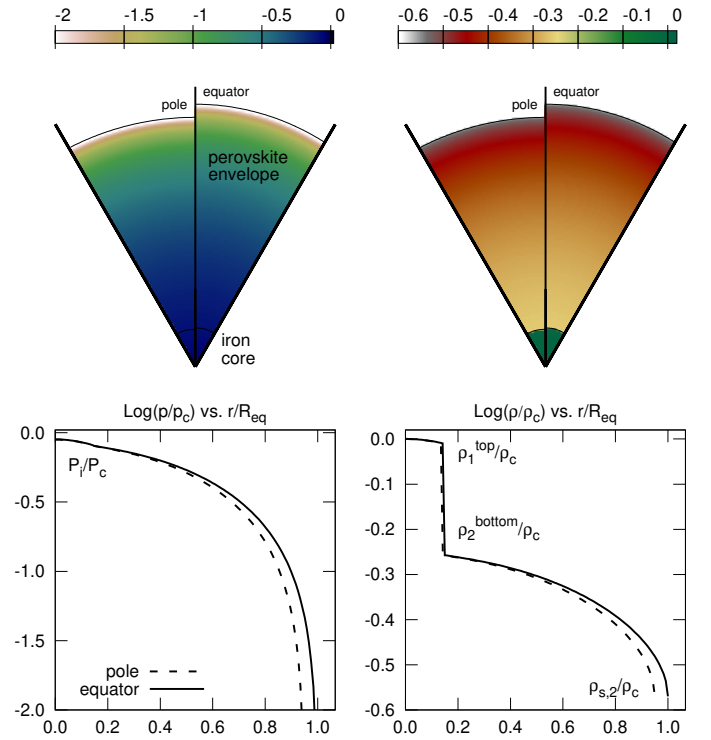


Fig. 15. Same caption as for Fig. 2 but for LHS 1140 b, assuming a rotating IP planet with $q = 0.15$ and $f = 0.05$; see also Tab. 5 and Fig. 13 (middle panel).

The PW hypothesis. This solution is relatively constrained in the sense that it persists only if f is very small according to Fig. 13 and Tab. 4. As quoted above, $f \leq \delta f \approx 0.038$. It means that LHS 1140 b can be a huge, slowly rotating silicate body with a shallow water envelope.

6.3. Discussion

The results presented above are in good agreement with the ternary diagrams presented in the spherical case in Daspute et al. (2024), based in the one-dimensional computational code by Zeng & Seager (2008) with updated EOS. These authors, actu-

Table 5. Input parameters and results for the two-layer, IP planet displayed in Fig. 15.

| | |
|--|---------|
| ▼ input | |
| flattening parameter f | 0.05 |
| $A = \rho_{s,2}/\rho_2^{\text{bottom}}$ | 0.4866 |
| relative core size (pole) q | 0.15 |
| ▼ output | |
| equatorial radius R_{eq} in R_{\oplus} | 1.7303 |
| estimated from the fit, i.e. Eq.(26) | 1.7145 |
| total mass M in M_{\oplus} | 5.5999 |
| relative mass of the core M_1/M | 0.0079 |
| mean mass-density $\langle\rho\rangle$ (g/cm ³) | 6.2717 |
| central-to-mean mass-density ratio $\rho_c/\langle\rho\rangle$ | 2.4284 |
| top-to-central mass density ratio (core) $\rho_1^{\text{top}}/\rho_c$ | 0.9763 |
| rotation period T (h) | 6.4036 |
| relative size of the core (equator) Q | 0.1479 |
| interface mass-density jump $\rho_1^{\text{top}}/\rho_2^{\text{bottom}} \equiv \alpha$ | 1.7649 |
| central-to-surface mass density ratio $\rho_c/\rho_{s,2}$ | 3.7147 |
| central pressure P_c (10 ⁹ dyn/cm ²) | 8470.46 |
| interface pressure $P_i \equiv P(Z_1)$ (10 ⁹ dyn/cm ²) | 7653.08 |

ally, do not rule out a two-layer structure for this planet, and the core mass-fractions predicted for the IW and PW configurations are similar to those reported in this work.

Although the IW-configuration is not really realistic, the large f -values presented in Fig. 14 better illustrate the additional degeneracies for the internal structure of such terrestrial planets when rotation is accounted for. For LHS 1140 b, they correspond to very small rotation periods of a few hours only (close to the critical angular velocity), which must be regarded as illustrative cases and cannot represent the genuine, current spin rate of LHS 1140 b. Indeed, this planet orbits at a short stellocentric distance (< 0.1 au), where the tidal locking time is expected to be much shorter than the system age of 5 Gyr. Its initial rotation must therefore have converged towards an equilibrium state between gravitational and thermal atmospheric tides, if any atmosphere is present (e.g. Leconte et al. 2015). Actually, for each composition of our double-layer model, we can estimate the maximum (‘primordial’) value of f compatible with the observational error bars (for instance, $f \approx 0.029$ corresponds to a minimum period $T \approx 7.5$ h for the IW case, see Fig.14).

Large spin rates are nevertheless not excluded for young, solid planets. In the current paradigm, giant impacts are expected to play a significant role at late stages of the planet formation process, and can spin-up planets close to their breakup velocity (e.g. Kokubo & Ida 2007; Miguel & Brunini 2010). In their recent collision scenario for the Earth-Moon system, to form the Moon from the Earth’s mantle, Čuk & Stewart (2012) even invoked a pre-impact spin rate of 2.3 h only for the proto-Earth. Pebble accretion is also thought to offer a valuable mechanism to significantly spin-up solid protoplanets through angular momentum transfer from the pebbles flow to the surface of the forming planet (Johansen & Lacerda 2010; Visser et al. 2020). Pebble accretion might be able to yield such fast (initial) rotation periods close to the critical breakup value for terrestrial planets (Takaoka et al. 2023), although recent developments suggest that the final outcome for the planetary spin strongly depends on the details of the modeling of the angular momentum transfer through the planet’s primordial atmosphere (Yzer et al. 2023). Due to a methodology bias and sensitivity limitation of the transit technique, studying spin distributions and constrain-

ing planetary oblateness remains limited to the gaseous giants, as no genuine super-Earth has been detected by the transit technique beyond the tidal locking region so far; see e.g. Liu et al. (2025) for Kepler167e, and Lammers & Winn (2024) for Kepler51d. Within the next decade, the PLATO mission (Rauer et al. 2024) is expected to populate this domain with dozens of Earth-like and Super-Earth planets with orbital periods long enough ($\gtrsim 100 - 200$ d) to escape tidal braking.

7. Summary, discussion and perspectives

7.1. Mass-radius-flattening relationships (summary)

In this paper, we have computed mass-radius relationships for single-layer and two-layer planets, including solid-body rotation by a conservative approach, leading to “mass-radius-flattening” relationships. We have selected three types of materials composing the core and the envelope, namely iron, perovskite and water, and the bimodal EOS from Seager et al. (2007). Tables of data are available in electronic form (see note 2); see Appendix A for a sample. Specific simulations can be performed upon request.

In the reference mass-range from 0.1 to 10 M_{\oplus} , the mass-radius relationships are, in log. scale, very well fitted by a quadratic law, and this is still possible when rotation is accounted for. Despite the fits are valid over only two decades in mass, these are fully reversible in any of the 3 parameters M , q and f . This is very useful to get rapid insight of permitted configurations, in terms of core size and rotational states. For single-layer planets, we can summarize the results as follows:

- the mass-radius relationships are given by Eq.(12) where the 9 coefficients c_{ij} are found in Tab. D.1,
- the inverse formula $f(M, R_{\text{eq}})$ is given by Eq.(18),
- in the static case, we have

$$R_{\text{eq}} \propto \begin{cases} M^{0.293 \pm 0.037} & \text{for iron planets,} \\ M^{0.301 \pm 0.030} & \text{for perovskite planets,} \\ M^{0.293 \pm 0.034} & \text{for water planets,} \end{cases} \quad (38)$$

- where the upper (lower) value refers to the lower (resp. upper) bound in the mass reference range,
- the relative change in the radius (at constant mass) and in the mass (at constant radius) due to rotation are $\eta_r f$ and $\eta_m f$, respectively; see Eqs. (14) and (16),
- the rotation period is available from Eq.(21), where the coefficients are listed in Tab. E.1,
- for a given mass, the central pressure is slightly decreased, which meets the result established in the single-layer, polytropic case by Chandrasekhar (1933a).

For two-layer planets, the core fractional size q is the additional parameter. The mass-radius-flattening relationships can still be fitted in this case, with a sigmoid for q . It follows that:

- the mass-radius relationships are described by Eq.(26), where the coefficients c'_{ij} , d_{ij} and σ are given in Tab. I.1,
- in the static case and for a given fractional core size q , we have from Eq.(28) and Tab. I.1,

$$R_{\text{eq}} \propto \begin{cases} M^{0.292 \pm 0.036} & \text{for IW planets,} \\ M^{0.299 \pm 0.031} & \text{for IP planets,} \\ M^{0.294 \pm 0.035} & \text{for PW planets,} \end{cases} \quad (39)$$

where the upper (lower) value refers to the lower (resp. upper) bound in the mass reference range.

Table 6. Effective index n_{eff} according to Eq.(40).

| \mathcal{L} | case | β | n_{eff} |
|---------------|-------------------|-------------------|---------------------------|
| 1 | iron planet | 0.293 ± 0.037 | $0.170^{+0.141}_{-0.156}$ |
| | perovskite planet | 0.301 ± 0.030 | $0.139^{+0.120}_{-0.131}$ |
| | water planet | 0.293 ± 0.034 | $0.171^{+0.132}_{-0.146}$ |
| 2 | IW planet | 0.292 ± 0.036 | $0.177^{+0.138}_{-0.153}$ |
| | IP planet | 0.299 ± 0.031 | $0.147^{+0.120}_{-0.131}$ |
| | PW planet | 0.294 ± 0.035 | $0.166^{+0.136}_{-0.150}$ |

- the relative change in the radius (at constant mass) and in the mass (at constant radius) due to rotation are found from $\eta_r f$ and $\eta_m f$, respectively; see Eqs. (30) and (31) and Fig. 8,
- for a given mass, radius and associated uncertainties ($x_0 \pm \delta x, y_0 \pm \delta y$), the relative size of the core (and uncertainty) can be determined from Eq.(33), and it depends on rotation (see for instance Fig. 11),
- in the limit of small flattenings, f can be expressed as a function of M, R_{eq} and q (this part is left to the reader),

The numerical suveys reveals that the relative change in the radius (mass) at constant mass (radius respectively) due to planet spin (see Sect. I.1), which is measured by the parameter $\eta_r f$ ($\eta_m f$ respectively) is significantly larger than for a rotating, homogeneous body. This is marginally significant for single-layer planet, but more pronounced for two-layer planets with core size $q \approx 0.70 \pm 0.05$ depending on the composition, as Fig. 8 shows.

7.2. Slope and "effective" polytropic index

As a direct consequence of the EOS, the power-law exponent is $\beta \approx 0.3$ for single and two-layer planets, for the mass range of reference. This is slightly larger than in Seager et al. (2007) who considered a wider range of reference, and in Boujibar et al. (2020), and more compatible with values extracted from exoplanet catalogs (Parc et al. 2024). This remains in good agreement with Fortney et al. (2007), both in terms of absolute position and slopes (slightly larger here), despite slight differences in the EOS (in particular ρ_s). We have seen that β depends on f , through the coefficient c_1 and $\langle c'_1 \rangle$, and is larger with rotation. It would therefore be very interesting to understand the individual role or effect of the three parameters ρ_s, A (i.e. K) and m in these laws, and more generally, to determine how the coefficients in the fits depend on these three parameters. In the static case, this can be performed directly from the Lane-Emden equation.

According to Eq.(22), a power-law of the form $R \propto M^\beta$ corresponds to a single-layer polytropic EOS with index

$$n = \frac{1 - 3\beta}{1 - \beta} \equiv n_{\text{eff}}. \quad (40)$$

As $\beta \approx 0.3$ in all cases presented in the article, the bimodal EOS corresponds to an "effective" polytropic index $n_{\text{eff}} \approx \frac{1}{7}$. Values of n_{eff} obtained for the single-layer and two-layer planet examined in the article are listed in Tab. 6. It means that the mass-radius relationships computed from Eq. (4) can be reproduced with a single layer polytrope with index n_{eff} . The fact that n_{eff} remains close to 0 means that the global internal structure is close to a piling of homogeneous layers, as mass density profiles show.

7.3. Note on the ocean depth of water-rich planets

When the outer layer is made of water, and the conditions are met at the surface for water to be in liquid phase, then we can

determine the depth d of the liquid ocean by considering the pressure and density at which phase transition to high pressure ice/ice VII occurs. This point in principle depends on temperature. As a typical/low value (Léger et al. 2004), we can take 10^{10} dyn/cm² $\equiv P_{\text{ref}}$ and solve $P(R, Z) = P_{\text{ref}}$ numerically for any structure computed with the DROP code. In contrast to the spherical case, d is expected to depend on the latitude. We can give an estimate of the ocean depth at the pole from the equation of hydrostatic equilibrium, namely

$$-P_{\text{ref}} = - \int_{R_{\text{pol}}-d}^{R_{\text{pol}}} \rho d\Psi, \quad (41)$$

and the impact of rotation. In the limit of small flattening values $f \rightarrow 0$, we have for any homogenous spheroid (e.g. Binney & Tremaine 1987)

$$\Psi(0, Z) \approx -\frac{2}{3}\pi G\rho \left[(3 - 2f)R_{\text{eq}}^2 - \left(1 + \frac{4}{5}f\right)Z^2 \right], \quad (42)$$

Assuming $d^2 \ll R_{\text{pol}}^2$ and that the effect of rotation on the gravitational acceleration in the surface layer is not greatly altered by spheroidal stratification with respect to the Maclaurin spheroid, we have $P_{\text{ref}} \approx \rho_s g [\Psi(R_{\text{pol}}) - \Psi(R_{\text{pol}} - d)]$. So, we find from Eq.(41)

$$P_{\text{ref}} \approx \frac{GM\rho_s d}{R_{\text{eq}}^2} \left(1 + \frac{4}{5}f\right), \quad (43)$$

and it follows that d decreases with the mass like $d \propto M^{2\beta-1}$, and decreases as rotation increases. By setting $P_{\text{ref}} \approx 10^{10}$ dyn/cm², we get

$$d_{\text{ref}} = \frac{P_{\text{ref}}R_{\oplus}^2}{GM_{\oplus}\rho_s} \approx 70 \text{ km}, \quad (44)$$

which is for a non-rotating planet with same size and mass as the Earth (note that this value is obviously sensitive to ρ_s , and we would get a 30% larger depth for $\rho_s = 1$ g/cm³). In the general case, we find

$$\log \frac{d}{d_{\text{ref}}} \approx 2y - x - \frac{4}{5}f, \quad (45)$$

and we can use Eq.(10) or (26) to get a function of x, q and f only. Note that the impact of rotation, which is weak, is not only supported by the term $\frac{4}{5}f$, but also by y which depends on f too. For LHS 1140 b, the ocean depth estimated from the DROP code is about 33 km in the static IW-case (see Fig. 14), while Eq. (45) predicts 37 km. We have verified that the depth at the equator is a little bit larger than at the pole, which is the consequence of the mass-density gradient, slightly weaker along the equatorial axis.

7.4. Corrections in the mass-radius relationships due to the planet oblateness and axis orientation

When the radius is deduced from transit method, the planet is generally assumed spherical, meaning that the obstacle to the star light seen by the observer is a circular disc. This is slightly different if the planet is spinning. Following Berardo & de Wit (2022), two extreme geometries of the primary eclipse can be considered, as sketched in Fig. 16:

- during a circular transit, the rotation axis is always oriented towards the observer (case b), then the blocking section is a disc, and the area is $\pi R_{\text{sp}}^2 = \pi R_{\text{eq}}^2$,

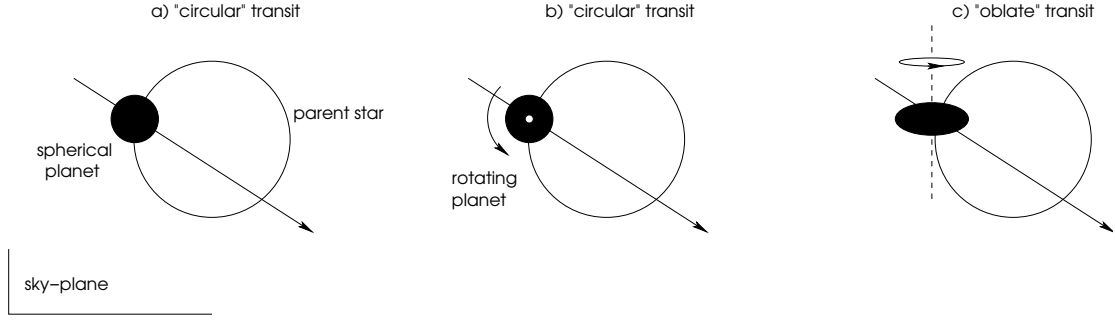


Fig. 16. Two extreme orientations of the rotation axis of the planet with respect to the line-of-sight (perpendicular to the figure) during a transit, relative to the spherical case.

- during an oblate transit, the rotation axis is always perpendicular to the line-of-sight (case c), then the relevant shape is roughly an elliptic disc, and the area is $\pi R_{\text{sph}}^2 = \pi R_{\text{eq}}^2 (1 - f)$.

Regarding photometric signals, there is no difference between a spherical planet (case a) and a pole-on, spinning planet (case b). In the latter situation, however, the position of the planet in the mass-radius relationship is higher than it would be in the static case, leaving the impression that the planet contains a larger fraction of light compounds. For an oblate-transit (case c), we have $R_{\text{sph}} = R_{\text{eq}} \sqrt{1 - f}$, which leads to

$$y_{\text{sph}} = y + \frac{1}{2} \log(1 - f) \quad (46)$$

with the same notation as for Eq.(26). In this case, without sufficient resolution to detect the rotation state at the ingress/egress of the transit, then the position of the planet in the mass-radius relationship based upon R_{sph} leaves the impression that the planet contains heavier elements, because it is in fact higher in the diagram. We see that the correction for an oblate transit in the mass-radius relationships can be accounted self-consistently for by inserting Eq.(46) into Eq.(33). We find

$$q = \left\{ \frac{y_{\text{sph}} - \frac{1}{2} \tau \log(1 - f) - c'_1 x - c'_2 x^2 - d_0}{d_1 - d_2 \left[y_{\text{sph}} - \frac{1}{2} \tau \log(1 - f) - c'_1 x - c'_2 x^2 \right]} \right\}^{\frac{1}{\sigma}}, \quad (47)$$

where we have introduced the parameter $\tau \in [0, 1]$ (i.e. it is zero for a circular transit and unity for an oblate transit).

For LHS 1140 b, an oblate transit means a larger equatorial radius. With $f = 0.05$ as considered in the figures, the “true” equatorial radius becomes $R_{\text{eq}} \approx 1.77$.

We show in Fig. 17 the effective position of LHS 1140 b in the PW-diagram with flattening $f = 0.05$, assuming an oblate transit, together with the A-sequence that crosses the new “effective” central value, i.e. $(x_0, y_{\text{sph}} - \frac{1}{2} \log(1 - f))$. In this case, the “true” equatorial radius becomes $R_{\text{eq}} \approx 1.77$. Figure 18 displays the structure corresponding to this new point, and Table 7 lists the new data for this equilibrium.

7.5. Three-layers and more

A natural continuation of this work is the introduction of new layers. A three-layer rotating planet made of an iron core, a silicate intermediate layer/mantle and a water envelope, i.e. an IPW planet, would be of particular interest for LHS 1140 b as it is located very close to a pure perovskite composition Valencia et al. (2007a). According to our analysis, the internal structure of LHS 1140 b is compatible with i) a small iron core surrounded

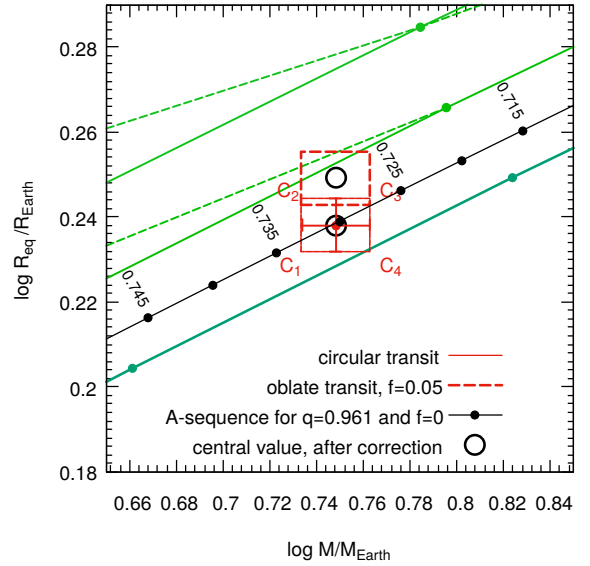


Fig. 17. Effective position of LHS 1140 b in the PW-diagram if the rotation axis of the planet is perpendicular to the line-of sight, corresponding to an oblate transit for $f = 0.05$; see also Figs. 13 (bottom) and 16.

Table 7. Input parameters and results (column 3) for the PW planet shown in Fig. 18, assuming an oblate transit and $f = 0.05$.

| ▼ input | | |
|---|---------|---------|
| flattening parameter f | 0* | 0.05 |
| $A = \rho_{s,2} / \rho_2^{\text{bottom}}$ | 0.7300 | 0.7108 |
| relative core size (pole) q | 0.9606 | 0.9524 |
| ▼ output | | |
| spherical radius R_{eq} in R_{\oplus} | 1.7317 | 1.7303 |
| equatorial radius R_{eq} in R_{\oplus} | 1.7317 | 1.7751 |
| total mass M in M_{\oplus} | 5.5932 | 5.6020 |
| relative mass of the core M_1 / M | 0.9656 | 0.9567 |
| mean mass-density $\langle \rho \rangle$ (g/cm^3) | 5.9413 | 5.8137 |
| $\rho_c / \langle \rho \rangle$ | 1.4584 | 1.4748 |
| $\rho_1^{\text{top}} / \rho_c$ | 0.5355 | 0.5478 |
| rotation period T (h) | – | 6.3523 |
| relative size of the core (equator) Q | 0.9605 | 0.9514 |
| $\rho_1^{\text{top}} / \rho_2^{\text{bottom}} \equiv \alpha$ | 2.3200 | 2.2868 |
| $\rho_c / \rho_{s,2}$ | 5.9347 | 5.8725 |
| central pressure P_c ($10^9 \text{ dyn}/\text{cm}^2$) | 8147.64 | 8147.61 |
| ocean depth (pole, km) | 30 | 30 |
| ocean depth (equator, km) | 30 | 33 |

*static case

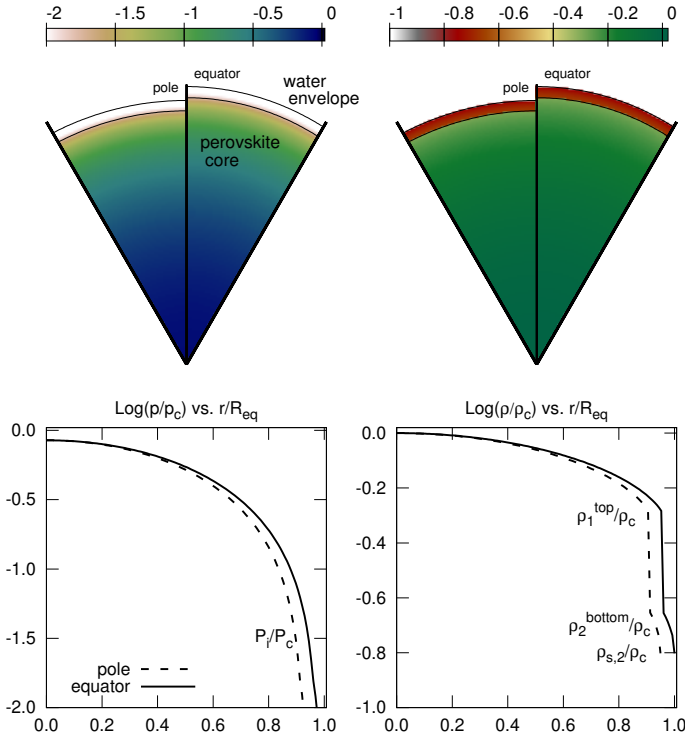


Fig. 18. Same caption as for Fig. 15 but assuming a PW planet and an oblate transit with $f = 0.05$ (period $T \approx 6$ h); see also Tab. 7 and Fig. 17.

by a large silicate mantle, and ii) a thin water surface layer on top of a big silicate core, as depicted in Figs. 15 and 18. Would a mixture of these two extreme configurations, in the form of a three-layer body, be plausible? As shown in Daspute et al. (2024), the silicate mantle should not occupy more 39% of the planet in size, to the benefit of the water and iron layers. This question merits indeed an extension of our approach to configurations with $\mathcal{L} = 3$. Considering an additional atmosphere, made of hydrogen and helium or water vapor for instance, and studying the response of a gas phase to rotation is another challenge to face (Adams et al. 2008).

Fitting the mass-radius relationship should become very complicated for $\mathcal{L} > 2$, because the number of parameters increases. Actually, each new layer requires two new parameters (the mass-density and the relative position with respect to the others). This addresses the question of the computing time. Accounting for more layers means is costly. With the modified polytropic EOS running the DROP code is already longer, in particular due to the special function (see Sect. B). It would be interesting to have both $H(\rho)$ and $\rho(H)$ available in the form of an approximation, for each index m of the EOS. A preliminary inspection shows that $1/2 F_1(u)$ can be very well fitted by a low-degree polynomial in $u \in [0, \frac{1}{2}]$. With a second-order polynomial, easily reversible, the relative precision is already as low as few 10^{-4} in relative. With such an option, some computing time is saved, and this would enable to increase the number of layers by maintaining the actual resolution. An alternative is to use the method of dimension reduction as proposed in Staelen & Huré (2024), which is currently under examination.

Acknowledgements. This research has made use of the NASA Exoplanet Archive, which is operated by the California Institute of Technology, under contract with the National Aeronautics and Space Administration under the Exoplanet Exploration Program (retrieved on Dec 13, 2024). This research has made

use of data obtained from or tools provided by the portal exoplanet.eu of The Extrasolar Planets Encyclopaedia. This work was supported by the Programme National de Planétologie (PNP) of CNRS-INSU co-funded by CNES. Computer time was provided by the computing facilities MCIA (Mésocentre de Calcul Intensif Aquitain) of the Université de Bordeaux. It is a pleasure to thank M. Turbet, F. Chambat and Y. Ricard for very interesting inputs and advices on the article prior to submission, and J. Leconte. We are grateful to the referee, Dr. A. Agüichine, for his very detailed report and the many criticisms, questions and suggestions to improve the article.

References

- Adams, E. R., Seager, S., & Elkins-Tanton, L. 2008, *ApJ*, 673, 1160
- Agol, E., Dorn, C., Grimm, S. L., et al. 2021, *The Planetary Science Journal*, 2, 1
- Agüichine, A., Mousis, O., Deleuil, M., & Marcq, E. 2021, *ApJ*, 914, 84
- Akeson, R. L., Chen, X., Ciardi, D., et al. 2013, *PASP*, 125, 989
- Akinsanmi, B., Barros, S. C. C., Santos, N. C., Oshagh, M., & Serrano, L. M. 2020, *Monthly Notices of the Royal Astronomical Society*, 497, 3484–3492
- Amendt, P., Lanza, A., & Abramowicz, M. A. 1989, *ApJ*, 343, 437
- Auclair-Desrotour, P., Farhat, M., Boué, G., Deitrick, R., & Laskar, J. 2024, arXiv e-prints, arXiv:2410.16200
- Barnes, R. 2017, *Celestial Mechanics and Dynamical Astronomy*, 129, 509
- Basillais, B. & Huré, J.-M. 2021, *MNRAS*, 506, 3773
- Berardo, D. & de Wit, J. 2022, *ApJ*, 935, 178
- Binney, J. & Tremaine, S. 1987, *Galactic dynamics* (Princeton, NJ, Princeton University Press, 1987, 747 p.)
- Boujibar, A., Driscoll, P., & Fei, Y. 2020, *Journal of Geophysical Research (Planets)*, 125, e06124
- Brinkman, C. L., Polanski, A. S., Huber, D., et al. 2024, arXiv e-prints, arXiv:2409.08361
- Brugger, B., Mousis, O., Deleuil, M., & Deschamps, F. 2017, *ApJ*, 850, 93
- Cadieux, C., Doyon, R., MacDonald, R. J., et al. 2024a, *ApJ*, 970, L2
- Cadieux, C., Plotnykov, M., Doyon, R., et al. 2024b, *ApJ*, 960, L3
- Canup, R. M. 2012, *Science*, 338, 1052
- Carado, B. & Knuth, K. 2020, *Astronomy and Computing*, 32, 100406
- Chandrasekhar, S. 1933a, *MNRAS*, 93, 390
- Chandrasekhar, S. 1933b, *MNRAS*, 93, 462
- Chandrasekhar, S. 1969, *Ellipsoidal figures of equilibrium* (Yale Univ. Press)
- Cox, J. P. & Giuli, R. T. 1968, *Principles of stellar structure Volume I : Physical principles*, 1st edn. (Gordon and Breach)
- Čuk, M. & Stewart, S. T. 2012, *Science*, 338, 1047
- Daspute, M., Wandel, A., Kopparapu, R. K., et al. 2024, arXiv e-prints, arXiv:2412.08476
- de Meijer, R., Anisichkin, V., & van Westrenen, W. 2013, *Chemical Geology*, 345, 40
- Dittmann, J. A., Irwin, J. M., Charbonneau, D., et al. 2017, *Nature*, 544, 333
- Dorn, C., Venturini, J., Khan, A., et al. 2017, *A&A*, 597, A37
- Dziewonski, A. M. & Anderson, D. L. 1981, *Physics of the Earth and Planetary Interiors*, 25, 297
- Edmondson, K., Norris, J., & Kerins, E. 2023, arXiv e-prints, arXiv:2310.16733
- Farinella, P., Davis, D. R., Paolicchi, P., Cellino, A., & Zappala, V. 1992, *A&A*, 253, 604
- Fortney, J. J., Marley, M. S., & Barnes, J. W. 2007, *ApJ*, 659, 1661
- Goldreich, P. & Peale, S. J. 1968, *ARA&A*, 6, 287
- Grasset, O., Schneider, J., & Sotin, C. 2009, *ApJ*, 693, 722
- Guillot, T. 1999, *Planet. Space Sci.*, 47, 1183
- Hachisu, I. 1986, *ApJS*, 61, 479
- Hakim, K., Rivoldini, A., Van Hoolst, T., et al. 2018, *Icarus*, 313, 61
- Haldemann, J., Alibert, Y., Mordasini, C., & Benz, W. 2020, *A&A*, 643, A105
- Haldemann, J., Dorn, C., Venturini, J., Alibert, Y., & Benz, W. 2024, *A&A*, 681, A96
- Haswell, C. A. 2010, *Transiting Exoplanets*
- Horedt, G. P., ed. 2004, *Astrophysics and Space Science Library*, Vol. 306, *Polytropes - Applications in Astrophysics and Related Fields*
- Houdayer, P. S. & Reese, D. R. 2023, *A&A*, 675, A181
- Howe, A. R., Burrows, A., & Verne, W. 2014, *ApJ*, 787, 173
- Huré, J.-M. & Hersant, F. 2017, *MNRAS*, 464, 4761
- Huré, J.-M., Hersant, F., & Nasello, G. 2018, *MNRAS*, 475, 63
- Johansen, A. & Lacerda, P. 2010, *MNRAS*, 404, 475
- Kadam, K., Motl, P. M., Frank, J., Clayton, G. C., & Marcelllo, D. C. 2016, *MNRAS*, 462, 2237
- Kellermann, C., Becker, A., & Redmer, R. 2018, *A&A*, 615, A39
- Kiuchi, K., Nagakura, H., & Yamada, S. 2010, *ApJ*, 717, 666
- Kokubo, E. & Ida, S. 2007, *ApJ*, 671, 2082
- Lammers, C. & Winn, J. N. 2024, *ApJ*, 977, L1
- Leconte, J., Wu, H., Menou, K., & Murray, N. 2015, *Science*, 347, 632
- Léger, A., Selsis, F., Sotin, C., et al. 2004, *Icarus*, 169, 499

- Lichtenberg, T. & Miguel, Y. 2025, *Treatise on Geochemistry*, 7, 51
- Lillo-Box, J., Figueira, P., Leleu, A., et al. 2020, *A&A*, 642, A121
- Liu, Q., Zhu, W., Masuda, K., et al. 2024, *ApJ*, 976, L14
- Liu, Q., Zhu, W., Zhou, Y., et al. 2025, *AJ*, 169, 79
- Ment, K., Dittmann, J. A., Astudillo-Defru, N., et al. 2019, *AJ*, 157, 32
- Miguel, Y. & Brunini, A. 2010, *MNRAS*, 406, 1935
- Mitra, V. 1977, *Mem. Soc. Astron. Italiana*, 48, 647
- Mousis, O., Deleuil, M., Aguichine, A., et al. 2020, *ApJ*, 896, L22
- Nettelmann, N., Fortney, J. J., Kramm, U., & Redmer, R. 2011, *ApJ*, 733, 2
- Nielsen, L. D. 2022, in *Disks and Planets across ESO Facilities*, 7
- Parc, L., Bouchy, F., Venturini, J., Dorn, C., & Helled, R. 2024, *A&A*, 688, A59
- Pearson, J. W., Olver, S., & Porter, M. A. 2014, arXiv e-prints, arXiv:1407.7786
- Rauer, H., Aerts, C., Cabrera, J., et al. 2024, arXiv e-prints, arXiv:2406.05447
- Ricard, Y. & Chambat, F. 2024, *ApJ*, 967, 163
- Rigby, F. E. & Madhusudhan, N. 2024, *MNRAS*, 529, 409
- Schubert, G., Anderson, J., Zhang, K., Kong, D., & Helled, R. 2011, *Physics of the Earth and Planetary Interiors*, 187, 364
- Schwieterman, E. W., Kiang, N. Y., Parenteau, M. N., et al. 2018, *Astrobiology*, 18, 663
- Seager, S., Kuchner, M., Hier-Majumder, C. A., & Militzer, B. 2007, *ApJ*, 669, 1279
- Slattery, W. L. 1977, *Icarus*, 32, 58
- Spiegel, D. S., Fortney, J. J., & Sotin, C. 2014, *Proceedings of the National Academy of Science*, 111, 12622
- Staelen, C. & Hurlé, J. M. 2024, *A&A*, 684, A59
- Swift, D. C., Eggert, J. H., Hicks, D. G., et al. 2012, *ApJ*, 744, 59
- Takaoka, K., Kuwahara, A., Ida, S., & Kurokawa, H. 2023, *A&A*, 674, A193
- Valencia, D., O'Connell, R. J., & Sasselov, D. 2006, *Icarus*, 181, 545
- Valencia, D., Sasselov, D. D., & O'Connell, R. J. 2007a, *ApJ*, 665, 1413
- Valencia, D., Sasselov, D. D., & O'Connell, R. J. 2007b, *ApJ*, 656, 545
- Vavrukh, M. V. & Dzikovskyi, D. V. 2020, *Contributions of the Astronomical Observatory Skalnaté Pleso*, 50, 748
- Verhoeven, O., Rivoldini, A., Vacher, P., et al. 2005, *Journal of Geophysical Research (Planets)*, 110, E04009
- Visser, R. G., Ormel, C. W., Dominik, C., & Ida, S. 2020, *Icarus*, 335, 113380
- Wagner, F. W., Tosi, N., Sohl, F., Rauer, H., & Spohn, T. 2012, *A&A*, 541, A103
- Wandel, A. 2018, *The Astrophysical Journal*, 856, 165
- Williams, P. S. 1988, *Ap&SS*, 143, 349
- Yunsheng Tian, B. & Stanley, S. 2013, *ApJ*, 768, 156
- Yzer, M. J., Visser, R. G., & Dominik, C. 2023, *A&A*, 678, A37
- Zahn, J. P. 1989, *A&A*, 220, 112
- Zapolsky, H. S. & Salpeter, E. E. 1969, *ApJ*, 158, 809
- Zeng, L., Sasselov, D. D., & Jacobsen, S. B. 2016, *ApJ*, 819, 127
- Zeng, L. & Seager, S. 2008, *PASP*, 120, 983
- Zhu, W., Huang, C. X., Zhou, G., & Lin, D. N. C. 2014, *ApJ*, 796, 67

Appendix A: Mass-radius-oblateness relationships for single-layer and two-layer planets

Table A.1. Example of data set* for a pure water planet with $f = 0.1$ (top) and for IW-planet with $f = 0.1$ and $q = 0.5$ (bottom).

| f | A | q | $\log R_{\text{eq}}/R_{\oplus}$ | $\log M/M_{\oplus}$ | M_1/M | $\langle \rho \rangle$ | $\rho_c/\langle \rho \rangle$ | $\rho_1^{\text{top}}/\rho_c$ | T | Q | α | $\rho_c/a_{\mathcal{L}}$ | $\log P_c$ | $\log P_1$ | C | m |
|-------|------|-----|---------------------------------|---------------------|---------|------------------------|-------------------------------|------------------------------|--------|--------|----------|--------------------------|------------|------------|--------|--------|
| 0.100 | 0.05 | 1.0 | +0.67404 | +2.29083 | 1.0000 | 11.3857 | 2.5646 | 0.0500 | 2.8976 | 1.0000 | 0.0500 | 20.0000 | 14.5484 | 14.5484 | 0.2967 | 0.1268 |
| 0.100 | 0.10 | 1.0 | +0.62909 | +1.92197 | 1.0000 | 6.6400 | 2.1988 | 0.1000 | 3.9229 | 1.0000 | 0.1000 | 10.0000 | 13.9159 | 13.9159 | 0.3159 | 0.1186 |
| 0.100 | 0.15 | 1.0 | +0.58704 | +1.66724 | 1.0000 | 4.9369 | 1.9715 | 0.1500 | 4.6556 | 1.0000 | 0.1500 | 6.6667 | 13.5242 | 13.5242 | 0.3288 | 0.1132 |
| 0.100 | 0.20 | 1.0 | +0.54624 | +1.45730 | 1.0000 | 4.0346 | 1.8094 | 0.2000 | 5.2421 | 1.0000 | 0.2000 | 5.0000 | 13.2293 | 13.2293 | 0.3387 | 0.1092 |
| 0.100 | 0.25 | 1.0 | +0.50571 | +1.26978 | 1.0000 | 3.4659 | 1.6850 | 0.2500 | 5.7385 | 1.0000 | 0.2500 | 4.0000 | 12.9858 | 12.9858 | 0.3467 | 0.1061 |
| 0.100 | 0.30 | 1.0 | +0.46471 | +1.09421 | 1.0000 | 3.0702 | 1.5851 | 0.3000 | 6.1718 | 1.0000 | 0.3000 | 3.3333 | 12.7730 | 12.7730 | 0.3534 | 0.1035 |
| 0.100 | 0.35 | 1.0 | +0.42265 | +0.92444 | 1.0000 | 2.7766 | 1.5024 | 0.3500 | 6.5598 | 1.0000 | 0.3500 | 2.8571 | 12.5798 | 12.5798 | 0.3592 | 0.1013 |
| 0.100 | 0.40 | 1.0 | +0.37898 | +0.75626 | 1.0000 | 2.4851 | 1.4322 | 0.4000 | 6.9115 | 1.0000 | 0.4000 | 2.5000 | 12.3990 | 12.3990 | 0.3643 | 0.0994 |
| 0.100 | 0.45 | 1.0 | +0.33310 | +0.58629 | 1.0000 | 2.2654 | 1.3716 | 0.4500 | 7.2334 | 1.0000 | 0.4500 | 2.2222 | 12.2256 | 12.2256 | 0.3688 | 0.0978 |
| 0.100 | 0.50 | 1.0 | +0.28433 | +0.41140 | 1.0000 | 2.2146 | 1.3185 | 0.5000 | 7.5325 | 1.0000 | 0.5000 | 2.0000 | 12.0557 | 12.0557 | 0.3729 | 0.0963 |
| 0.100 | 0.55 | 1.0 | +0.23184 | +0.22834 | 1.0000 | 2.0877 | 1.2715 | 0.5500 | 7.8117 | 1.0000 | 0.5500 | 1.8182 | 11.8859 | 11.8859 | 0.3766 | 0.0950 |
| 0.100 | 0.60 | 1.0 | +0.17456 | +0.03334 | 1.0000 | 1.9793 | 1.2294 | 0.6000 | 8.0740 | 1.0000 | 0.6000 | 1.6667 | 11.7125 | 11.7125 | 0.3800 | 0.0938 |
| 0.100 | 0.65 | 1.0 | +0.11101 | -0.17841 | 1.0000 | 1.8853 | 1.1914 | 0.6500 | 8.3215 | 1.0000 | 0.6500 | 1.5385 | 11.5317 | 11.5317 | 0.3832 | 0.0927 |
| 0.100 | 0.70 | 1.0 | +0.03909 | -0.41356 | 1.0000 | 1.8028 | 1.1569 | 0.7000 | 8.5562 | 1.0000 | 0.7000 | 1.4286 | 11.3384 | 11.3384 | 0.3861 | 0.0917 |
| 0.100 | 0.75 | 1.0 | -0.04443 | -0.68206 | 1.0000 | 1.7298 | 1.1254 | 0.7500 | 8.7795 | 1.0000 | 0.7500 | 1.3333 | 11.1257 | 11.1257 | 0.3889 | 0.0907 |
| 0.100 | 0.80 | 1.0 | -0.14495 | -1.00029 | 1.0000 | 1.6646 | 1.0964 | 0.8000 | 8.9952 | 1.0000 | 0.8000 | 1.2500 | 10.8821 | 10.8821 | 0.3914 | 0.0898 |
| 0.100 | 0.85 | 1.0 | -0.27252 | -1.39857 | 1.0000 | 1.6059 | 1.0696 | 0.8500 | 9.1994 | 1.0000 | 0.8500 | 1.1765 | 10.5873 | 10.5873 | 0.3938 | 0.0890 |
| 0.100 | 0.90 | 1.0 | -0.44971 | -1.94474 | 1.0000 | 1.5528 | 1.0447 | 0.9000 | 9.3954 | 1.0000 | 0.9000 | 1.1111 | 10.1956 | 10.1956 | 0.3961 | 0.0883 |
| 0.100 | 0.95 | 1.0 | -0.74846 | -2.85473 | 1.0000 | 1.5043 | 1.0216 | 0.9500 | 9.5839 | 1.0000 | 0.9500 | 1.0526 | 9.5630 | 9.5630 | 0.3983 | 0.0875 |

| f | A | q | $\log R_{\text{eq}}/R_{\oplus}$ | $\log M/M_{\oplus}$ | M_1/M | $\langle \rho \rangle$ | $\rho_c/\langle \rho \rangle$ | $\rho_1^{\text{top}}/\rho_c$ | T | Q | α | $\rho_c/a_{\mathcal{L}}$ | $\log P_c$ | $\log P_1$ | C | m |
|-------|------|-----|---------------------------------|---------------------|---------|------------------------|-------------------------------|------------------------------|--------|--------|----------|--------------------------|------------|------------|--------|--------|
| 0.100 | 0.05 | 0.5 | +0.56893 | +2.21668 | 0.4838 | 19.8835 | 6.8295 | 0.4272 | 1.9507 | 0.4721 | 1.9865 | 93.0093 | 15.3232 | 14.5484 | 0.2191 | 0.1606 |
| 0.100 | 0.10 | 0.5 | +0.53122 | +1.83751 | 0.4537 | 10.7733 | 5.9289 | 0.4906 | 2.7212 | 0.4734 | 2.1463 | 43.7488 | 14.6402 | 13.9159 | 0.2369 | 0.1523 |
| 0.100 | 0.15 | 0.5 | +0.49057 | +1.57024 | 0.4378 | 7.7085 | 5.4176 | 0.5414 | 3.2731 | 0.4739 | 2.3228 | 28.6037 | 14.2230 | 13.5242 | 0.2482 | 0.1471 |
| 0.100 | 0.20 | 0.5 | +0.44874 | +1.34740 | 0.4285 | 6.1594 | 5.0773 | 0.5851 | 3.7094 | 0.4742 | 2.5066 | 21.4199 | 13.9136 | 13.2293 | 0.2562 | 0.1433 |
| 0.100 | 0.25 | 0.5 | +0.40589 | +1.14697 | 0.4228 | 5.2192 | 4.8301 | 0.6242 | 4.0713 | 0.4746 | 2.6945 | 17.2669 | 13.6616 | 12.9858 | 0.2623 | 0.1403 |
| 0.100 | 0.30 | 0.5 | +0.36173 | +0.95849 | 0.4197 | 4.5871 | 4.6387 | 0.6599 | 4.3811 | 0.4758 | 2.8851 | 14.5742 | 13.4439 | 12.7730 | 0.2671 | 0.1379 |
| 0.100 | 0.35 | 0.5 | +0.31640 | +0.77662 | 0.4173 | 4.1270 | 4.4892 | 0.6930 | 4.6502 | 0.4759 | 3.0778 | 12.6896 | 13.2479 | 12.5798 | 0.2711 | 0.1360 |
| 0.100 | 0.40 | 0.5 | +0.26908 | +0.59648 | 0.4161 | 3.7791 | 4.3652 | 0.7240 | 4.8886 | 0.4762 | 3.2721 | 11.2990 | 13.0659 | 12.3990 | 0.2743 | 0.1344 |
| 0.100 | 0.45 | 0.5 | +0.21954 | +0.41504 | 0.4153 | 3.5039 | 4.2627 | 0.7533 | 5.1018 | 0.4763 | 3.4677 | 10.2303 | 12.8922 | 12.2256 | 0.2771 | 0.1331 |
| 0.100 | 0.50 | 0.5 | +0.16710 | +0.22924 | 0.4149 | 3.2814 | 4.1754 | 0.7810 | 5.2944 | 0.4763 | 3.6645 | 9.3845 | 12.7229 | 12.0557 | 0.2795 | 0.1319 |
| 0.100 | 0.55 | 0.5 | +0.11080 | +0.03546 | 0.4150 | 3.0980 | 4.0992 | 0.8073 | 5.4690 | 0.4765 | 3.8622 | 8.6979 | 12.5540 | 11.8859 | 0.2816 | 0.1310 |
| 0.100 | 0.60 | 0.5 | +0.04990 | -0.16963 | 0.4151 | 2.9424 | 4.0338 | 0.8325 | 5.6301 | 0.4763 | 4.0608 | 8.1296 | 12.3821 | 11.7125 | 0.2834 | 0.1301 |
| 0.100 | 0.65 | 0.5 | -0.01730 | -0.39117 | 0.4156 | 2.8102 | 3.9752 | 0.8566 | 5.7797 | 0.4765 | 4.2603 | 7.6515 | 12.2031 | 11.5317 | 0.2850 | 0.1292 |
| 0.100 | 0.70 | 0.5 | -0.09283 | -0.63585 | 0.4161 | 2.6955 | 3.9234 | 0.8797 | 5.9188 | 0.4765 | 4.4606 | 7.2435 | 12.0118 | 11.3384 | 0.2865 | 0.1285 |
| 0.100 | 0.75 | 0.5 | -0.17991 | -0.91358 | 0.4168 | 2.5952 | 3.8770 | 0.9019 | 6.0474 | 0.4765 | 4.6617 | 6.8914 | 11.8012 | 11.1257 | 0.2877 | 0.1278 |
| 0.100 | 0.80 | 0.5 | -0.28395 | -1.24074 | 0.4176 | 2.5066 | 3.8353 | 0.9233 | 6.1665 | 0.4765 | 4.8637 | 6.5847 | 11.5600 | 10.8821 | 0.2889 | 0.1273 |
| 0.100 | 0.85 | 0.5 | -0.41500 | -1.64776 | 0.4184 | 2.4279 | 3.7978 | 0.9438 | 6.2789 | 0.4765 | 5.0666 | 6.3155 | 11.2675 | 10.5873 | 0.2899 | 0.1268 |
| 0.100 | 0.90 | 0.5 | -0.59564 | -2.20246 | 0.4193 | 2.3574 | 3.7641 | 0.9635 | 6.3854 | 0.4765 | 5.2706 | 6.0778 | 10.8785 | 10.1956 | 0.2908 | 0.1262 |
| 0.100 | 0.95 | 0.5 | -0.89781 | -3.12080 | 0.4204 | 2.2941 | 3.7343 | 0.9824 | 6.4830 | 0.4765 | 5.4761 | 5.8676 | 10.2486 | 9.5630 | 0.2917 | 0.1258 |

*From left to right : the flattening parameter $f = 1 - R_{\text{pol}}/R_{\text{eq}} \geq 0$, where R_{pol} is the polar radius, and R_{eq} the equatorial radius, the A-parameter, where $\mathcal{L} \in \{1, 2\}$ is the number of layer, the relative size $q = Z_1/R_{\text{pol}}$ of the core along the axis of rotation, the decimal log. of the equatorial radius R_{eq} of the planet in units of the Earth's radius, with $R_{\oplus} = 6.371 \times 10^8$ cm, the decimal log. of the total mass M of the planet in units of the Earth's mass, with $M_{\oplus} = 5.972 \times 10^{27}$ g, the relative mass of the core M_1/M , the mean mass-density $\langle \rho \rangle = M/V$ in g/cm^3 , where V is the volume of the planet, the decimal log. of the central-to-mean mass-density ratio $\rho_c/\langle \rho \rangle$, the top-to-central mass density ratio in the core $\rho_1^{\text{top}}/\rho_c$, the rotation period T in h, the relative size $Q = R_1/R_{\text{eq}}$ of the core at the equator, the interface mass-density jump $\alpha \equiv \rho_1^{\text{top}}/\rho_2^{\text{bottom}}$, the central-to-surface mass density ratio $\rho_c/a_{\mathcal{L}}$, which is identical to $1/A$ in the single-layer case, the decimal log. of the central pressure P_c in dyn/cm^2 , the decimal log. of the interface pressure $P_1 \equiv P(Z_1)$ in dyn/cm^2 , the normalized moment of inertia $C = I_z/MR_{\text{eq}}^2$, and the m -parameter defined by $m = \Omega^2 R_{\text{eq}}^3/GM$. We take $G = 6.67259 \times 10^{-8}$ for the constant of gravitation.

Appendix B: Note on the hypergeometric function

As $0 \leq u \leq 1 - A < 1$ and $\gamma \approx 2$ in Eq.(6) for all the materials considered in this study (see Tab. 1), we can compute the special function ${}_2F_1(u) \equiv {}_2F_1(\gamma, \gamma; \gamma + 1; u)$ by direct summation of the terms of the Taylor series (Pearson et al. 2014). The function ${}_2F_1(u)$ associated with an iron layer is plotted in Fig. B.1 as an illustration. Convergence at the machine capability (16 digits in double precision) is easy and it requires no more than about a hundred terms for $u \leq \frac{1}{2}$, as indicated in Fig. B.1. Above this value, acceleration is necessary, especially when A is very close to zero. Convergence acceleration is obtained by performing a linear transformation $v = 1 - u$, leaving two hypergeometric functions to estimate. In practical, the switch can therefore be set a little bit beyond $u = \frac{1}{2}$ (see again Fig. B.1). So, whatever the argument $u \in [0, 1]$, the number of terms in the series remains relatively small (this number is divided by two typically for 8 digits). The second point concerns the Poisson equation. As a matter of fact, the mass density $\rho(H)$ is required in Eq.(2), which means that the function $H(\rho)$ defined by Eq.(6) must be reversed at each node of the computational grid (there are $N \times N$ effective nodes in total). This inversion is performed from a standard root-finding method, which involves iterations. We estimate that the computational cost is increased by a factor 3 at the actual resolution, depending also on A , and therefore on u ; see Sec. 7.

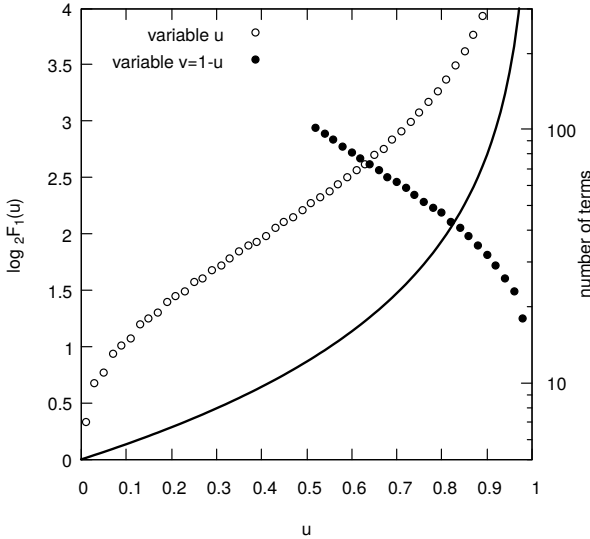


Fig. B.1. Decimal logarithm of the hypergeometric function ${}_2F_1(u)$ (black line) appearing in Eq.(6), and total number of terms in the Taylor series required to reach the computer precision, i.e. 16 digits (right axis). This number can be reduced by a factor two for a 8-digit precision; see Sec. B. The parameter is $\gamma \approx 1.89$ corresponding to iron (see Tab. 1).

Appendix C: Coefficients c_i fitting the mass-radius relationship for single-layer planets (static case)

Table C.1. Coefficients in Eq.(10) for iron.

| f | c_0 | c_1 | c_2 |
|-------|------------|------------|------------|
| 0.000 | -0.1010692 | +0.2933718 | -0.0183969 |
| 0.025 | -0.0970511 | +0.2937060 | -0.0183842 |
| 0.050 | -0.0929222 | +0.2940590 | -0.0183700 |
| 0.075 | -0.0886769 | +0.2944307 | -0.0183515 |
| 0.100 | -0.0843095 | +0.2948240 | -0.0183267 |
| 0.125 | -0.0798110 | +0.2952435 | -0.0182961 |
| 0.150 | -0.0751747 | +0.2956862 | -0.0182632 |
| 0.175 | -0.0703849 | +0.2961575 | -0.0182384 |
| 0.200 | -0.0654405 | +0.2966548 | -0.0182092 |

Table C.2. Coefficients in Eq.(10) for perovskite.

| f | c_0 | c_1 | c_2 |
|-------|------------|------------|------------|
| 0.000 | +0.0105525 | +0.3010068 | -0.0152134 |
| 0.025 | +0.0145022 | +0.3012828 | -0.0152036 |
| 0.050 | +0.0185591 | +0.3015741 | -0.0151921 |
| 0.075 | +0.0227294 | +0.3018809 | -0.0151778 |
| 0.100 | +0.0270190 | +0.3022045 | -0.0151612 |
| 0.125 | +0.0314328 | +0.3025494 | -0.0151343 |
| 0.150 | +0.0359814 | +0.3029146 | -0.0151063 |
| 0.175 | +0.0406767 | +0.3033038 | -0.0150817 |
| 0.200 | +0.0455257 | +0.3037160 | -0.0150580 |

Table C.3. Coefficients in Eq.(10) for water.

| f | c_0 | c_1 | c_2 |
|-------|------------|------------|------------|
| 0.000 | +0.1483488 | +0.2929427 | -0.0172455 |
| 0.025 | +0.1523712 | +0.2932570 | -0.0172342 |
| 0.050 | +0.1565050 | +0.2935890 | -0.0172216 |
| 0.075 | +0.1607556 | +0.2939389 | -0.0172051 |
| 0.100 | +0.1651294 | +0.2943090 | -0.0171844 |
| 0.125 | +0.1696342 | +0.2947054 | -0.0171555 |
| 0.150 | +0.1742802 | +0.2951243 | -0.0171287 |
| 0.175 | +0.1790761 | +0.2955672 | -0.0171043 |
| 0.200 | +0.1840293 | +0.2960352 | -0.0170789 |

Appendix D: Coefficients c_{ij} fitting the mass-radius relationship for single-layer planets

Table D.1. Coefficients c_{ij} for the mass-radius relationship fitted with Eq.(12) for single-layer planet, with rotation*.

| | $j = 0$ | $j = 1$ | $j = 2$ |
|--------------|-------------------|-------------------|------------|
| ▼ iron | | | |
| c_{0j} | -0.1010472 | +0.1568129 | +0.1055179 |
| c_{1j} | +0.2933768 | +0.0125997 | +0.0188474 |
| c_{2j} | -0.0183993 | +0.0005275 | +0.0022197 |
| ▼ perovskite | | | |
| c_{0j} | +0.0105736 | +0.1542161 | +0.1021337 |
| c_{1j} | +0.3010116 | +0.0103719 | +0.0156375 |
| c_{2j} | -0.0152144 | +0.0003446 | +0.0022846 |
| ▼ water | | | |
| c_{0j} | +0.1483707 | +0.1569754 | +0.1060086 |
| c_{1j} | +0.2929471 | +0.0118541 | +0.0178539 |
| c_{2j} | -0.0172474 | +0.0004563 | +0.0020234 |

*The exponent of the power-law for a static, one Earth's mass body is indicated (*bold*), as well as the linear contribution of rotation (*red*).

Appendix E: Coefficients t_{ij} fitting the period for single-layer planets

Table E.1. Coefficients t_{ij} for the mass-period relationship fitted with Eq.(21) for single-layer planet, with rotation.

| | $j = 0$ | $j = 1$ |
|--------------|------------|------------|
| ▼ iron | | |
| t_{0j} | +0.3594785 | -0.3414377 |
| t_{1j} | -0.0277489 | -0.0021638 |
| t_{2j} | -0.0117303 | -0.0045039 |
| ▼ perovskite | | |
| t_{0j} | +0.3661880 | -0.3409544 |
| t_{1j} | -0.0220200 | +0.0008478 |
| t_{2j} | -0.0128245 | -0.0049271 |
| ▼ water | | |
| t_{0j} | +0.3577173 | -0.3370310 |
| t_{1j} | -0.0273110 | -0.0012598 |
| t_{2j} | -0.0102134 | -0.0054784 |

Appendix F: Mass-radius relationship for two-layer, IP planets

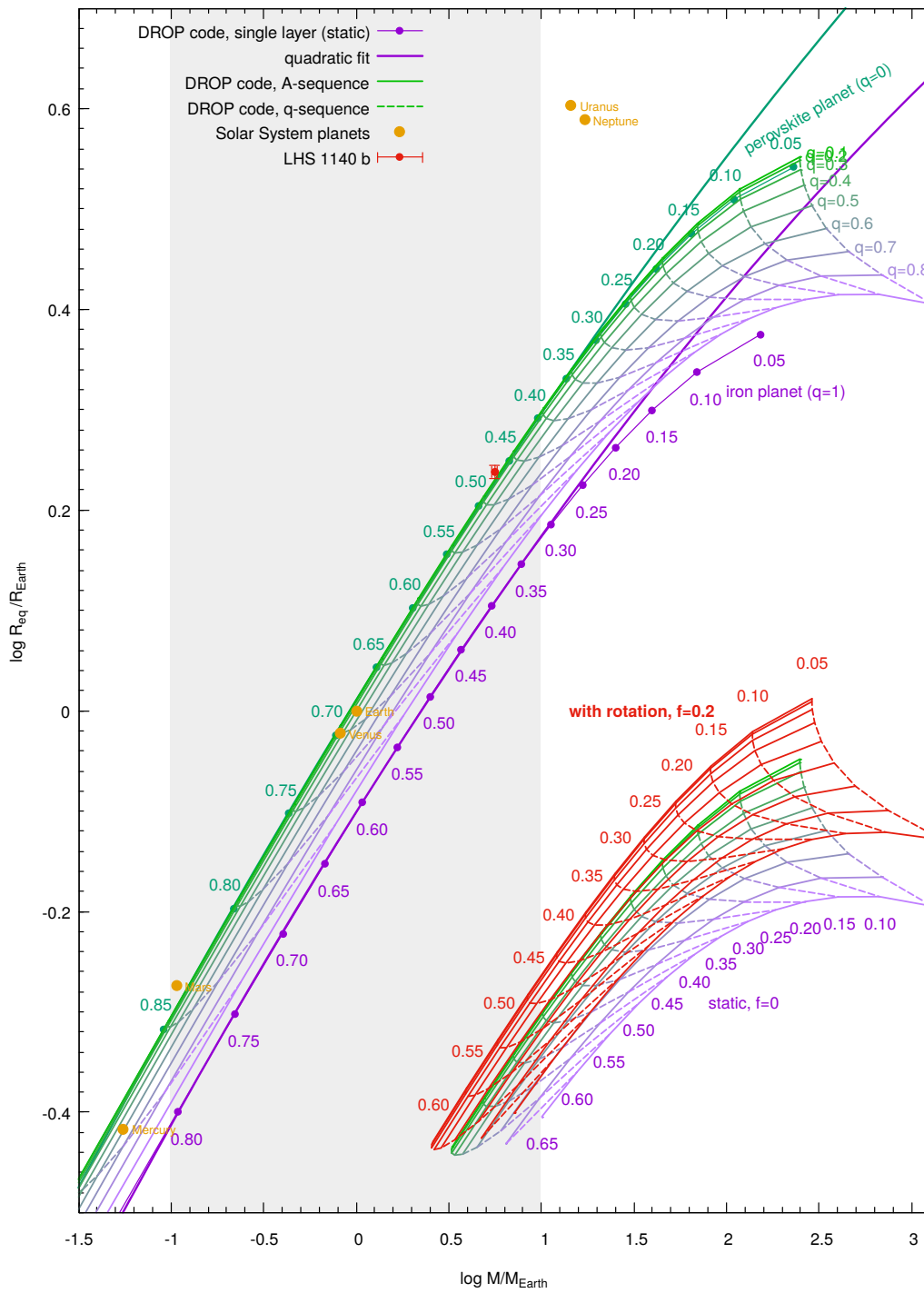


Fig. F.1. Same caption as for Fig. 6 but in a two-layer IP-planet.

Appendix G: Mass-radius relationship for two-layer, PW planets

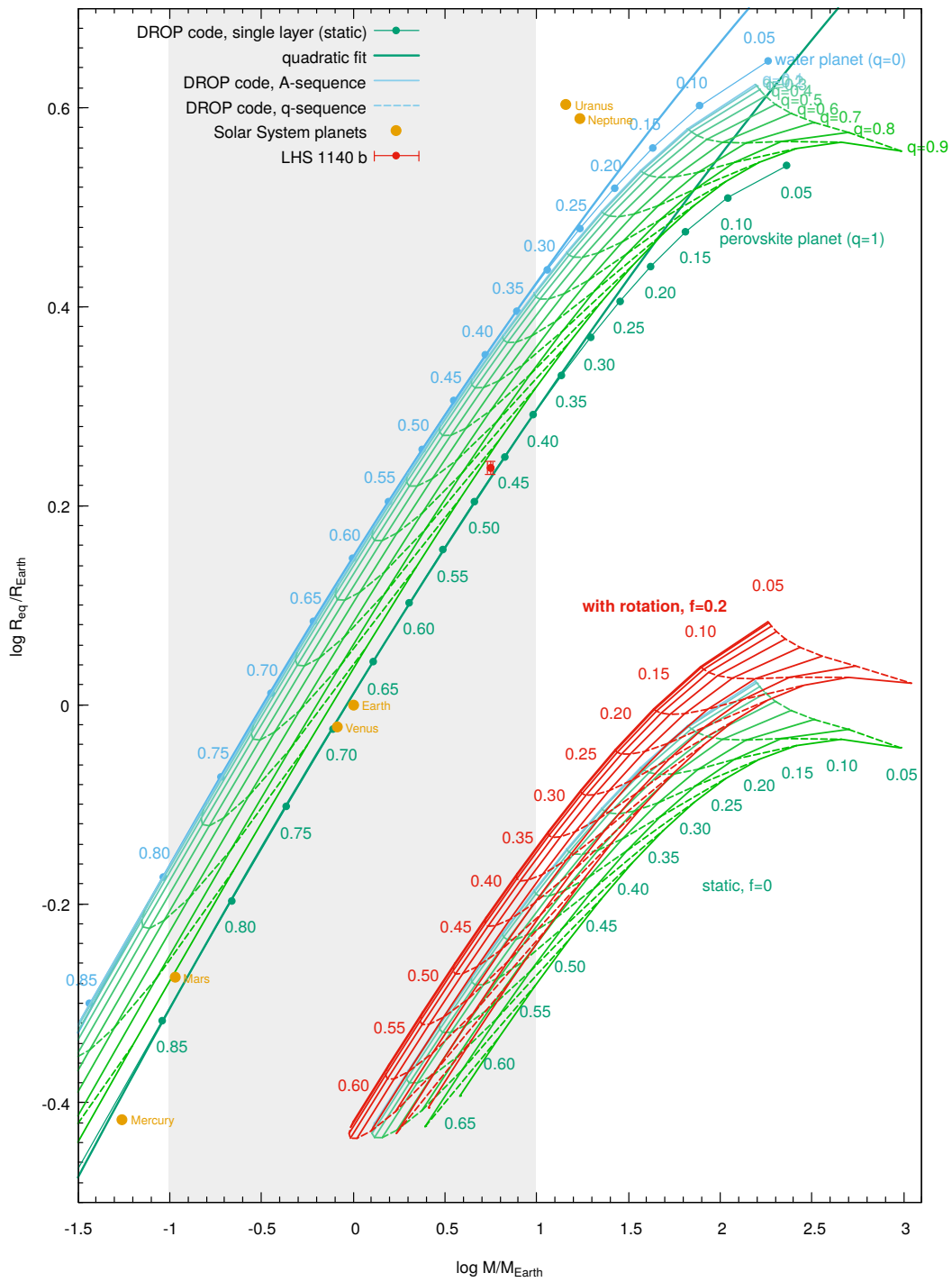


Fig. G.1. Same caption as for Fig. 6 but in a two-layer PW-planet.

Appendix H: Coefficients fitting the mass-radius relationship for two-layer, IW planets

Table H.1. Coefficients c'_i for the mass-radius relationship fitted with a quadratic law for a two-layer, IW planet for different values of q , in the static case*.

| q | c'_0 | c'_1 | c'_2 |
|------------------------|------------|------------|------------|
| 0.000 | +0.1483488 | +0.2929427 | -0.0172455 |
| 0.100 | +0.1461391 | +0.2931076 | -0.0174334 |
| 0.200 | +0.1415536 | +0.2923524 | -0.0182351 |
| 0.300 | +0.1290441 | +0.2917313 | -0.0176743 |
| 0.400 | +0.1076532 | +0.2908377 | -0.0178216 |
| 0.500 | +0.0786889 | +0.2900709 | -0.0187472 |
| 0.600 | +0.0444794 | +0.2906534 | -0.0184779 |
| 0.700 | +0.0079287 | +0.2901063 | -0.0183598 |
| 0.800 | -0.0291855 | +0.2924474 | -0.0182362 |
| 0.900 | -0.0656371 | +0.2935405 | -0.0181483 |
| $\langle c'_i \rangle$ | +0.0622961 | +0.2916497 | -0.0181260 |
| Δ_i | +0.1058881 | +0.0017348 | +0.0006569 |

*Values obtained for the pure-water planet (*first row*) have been copied from Tabs. C.1 to C.3. Mean values $\langle c'_i \rangle$ and half-amplitude Δ_i defined by Eq.(23) are also given.

Table H.2. Coefficients d_0 , d_1 , and d_2 for the sigmoidal representation of $c'_0(q)$ for the IW planet, assuming σ is a constant.

| f | d_0 | d_1 | d_2 |
|-------|------------|------------|------------|
| 0.000 | +0.1476811 | -0.3621996 | +1.1962805 |
| 0.025 | +0.1517282 | -0.3544016 | +1.1517880 |
| 0.050 | +0.1557795 | -0.3452736 | +1.0779073 |
| 0.075 | +0.1600821 | -0.3371772 | +1.0164078 |
| 0.100 | +0.1646047 | -0.3298797 | +0.9572348 |
| 0.125 | +0.1690640 | -0.3221491 | +0.8844918 |
| 0.150 | +0.1738964 | -0.3152371 | +0.8130963 |
| 0.175 | +0.1787665 | -0.3087314 | +0.7462931 |
| 0.200 | +0.1838491 | -0.3025681 | +0.6676232 |

Appendix I: Coefficients fitting the mass-radius relationship for two-layer, IW-, IP- and PW-planets

Table I.1. Coefficients* c'_{ij} , d_{ij} and σ .

| | $j = 0$ | $j = 1$ | $j = 2$ |
|--------------------|-------------------|-------------------|------------|
| ▼ IW-planet | | | |
| c'_{1j} | +0.2916497 | +0.0116867 | +0.0252880 |
| c'_{2j} | -0.0181260 | +0.0055022 | - |
| d_{0j} | +0.1476811 | +0.1563921 | +0.1218398 |
| d_{1j} | -0.3621996 | +0.3509368 | -0.2597847 |
| d_{2j} | +1.1962807 | -2.1953340 | -2.2445208 |
| σ | +2.7354873 | | |
| ▼ IP-planet | | | |
| c'_{1j} | +0.2990242 | +0.0141426 | +0.0102229 |
| c'_{2j} | -0.0153046 | +0.0052181 | - |
| d_{0j} | +0.0109148 | +0.1547714 | +0.1031154 |
| d_{1j} | -0.1653664 | +0.1488079 | +0.0098217 |
| d_{2j} | +0.5304047 | -0.6630659 | -2.1148875 |
| σ | +2.9477349 | | |
| ▼ PW-planet | | | |
| c'_{1j} | +0.2944043 | +0.0120350 | +0.0067155 |
| c'_{2j} | -0.0176780 | +0.0144473 | - |
| d_{0j} | +0.1460727 | +0.1501963 | +0.1318709 |
| d_{1j} | -0.1261723 | +0.0475825 | -0.2442127 |
| d_{2j} | +0.5988696 | -1.4232417 | -0.3751630 |
| σ | +2.8544981 | | |

*The exponent of the power-law for a static, one Earth's mass body is indicated (*bold*), as well as the linear contribution of rotation (*red*).

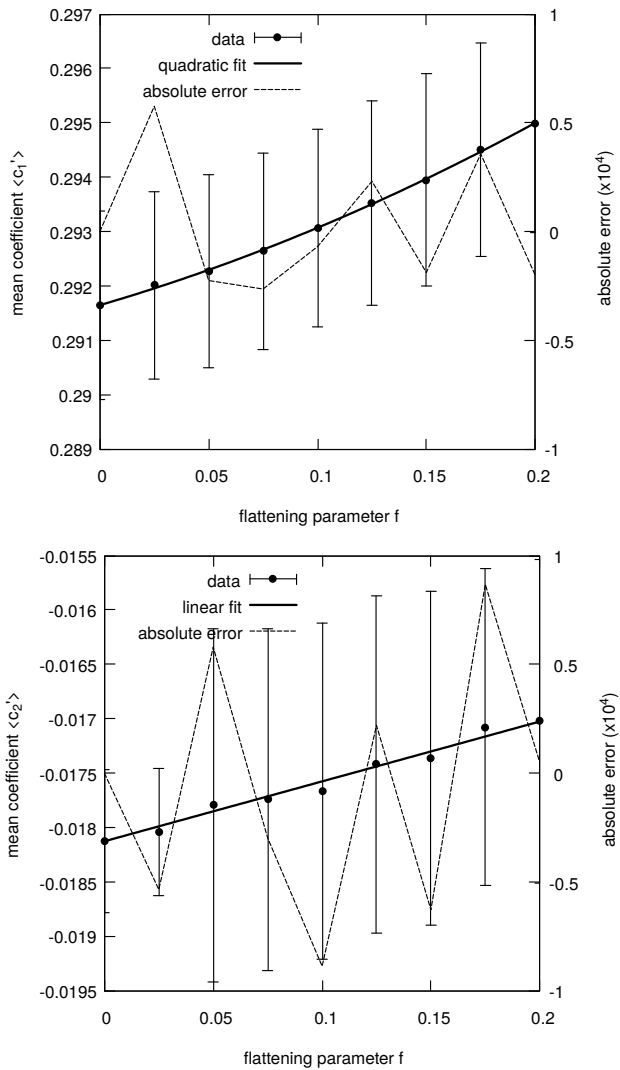


Fig. I.1. Mean coefficients $\langle c'_1 \rangle \pm \Delta_1$ (top) and $\langle c'_2 \rangle \pm \Delta_2$ (bottom) of the mass-radius relationship for a two-layer IW planet versus the flattening parameter f , the fits (plain lines) and the absolute errors in fitting the means (dashed-lines, right axis).

Appendix J: Central pressure and rotation periods for the IP and PW-planets

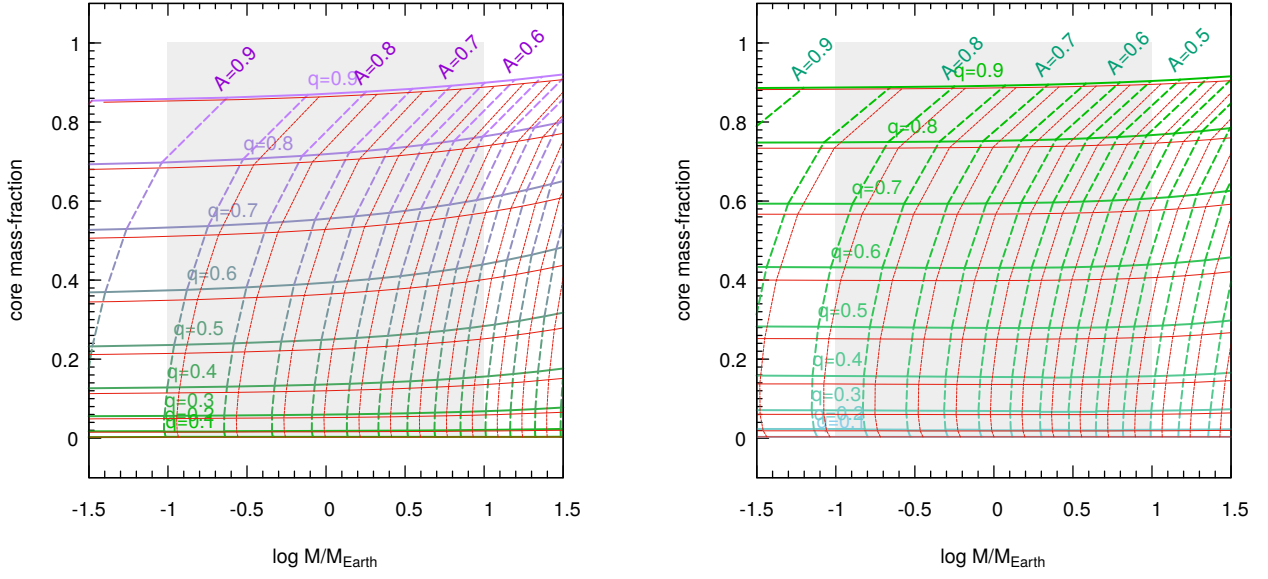


Fig. J.1. Same caption as for Fig. 9, but for the IP planet (left) and for the PW planet (right).

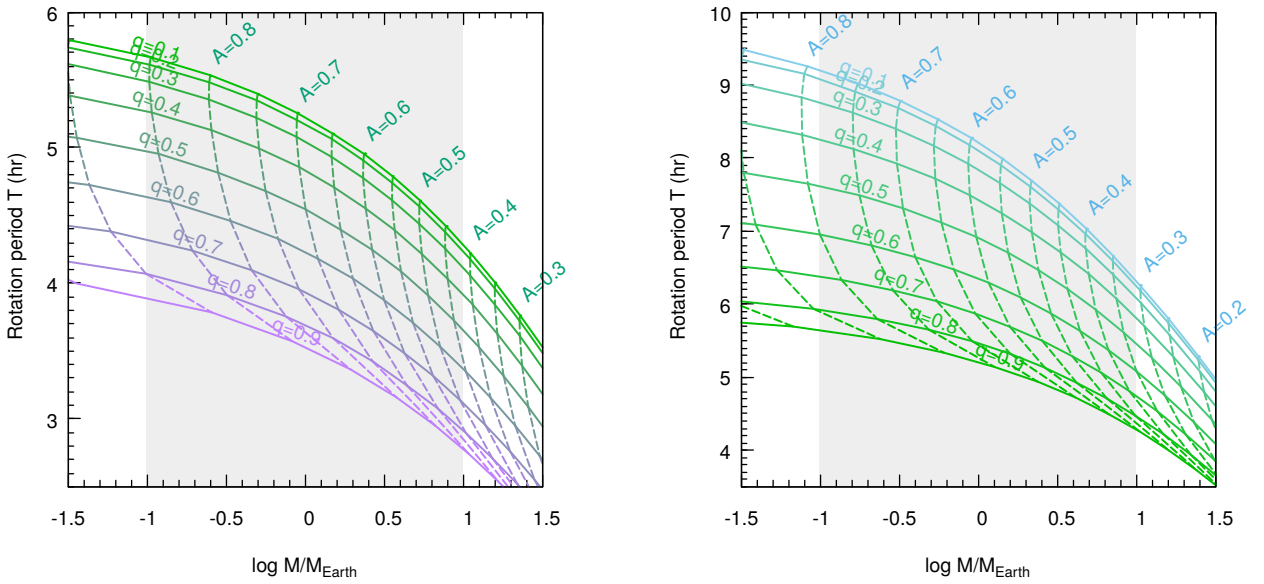


Fig. J.2. Same caption as for Fig. 10, but for the IP planet (left) and for the PW planet (right).